

# **Solar Eruptive Events:**

## **Coronal Dimming and a New CubeSat Mission**

by

**James Paul Mason**

B.S., University of California at Santa Cruz, 2009

M.S., University of Colorado at Boulder, 2012

A thesis submitted to the  
Faculty of the Graduate School of the  
University of Colorado in partial fulfillment  
of the requirements for the degree of  
Doctor of Philosophy  
Department of Aerospace Engineering Sciences  
2016

This thesis entitled:  
**Solar Eruptive Events:**  
Coronal Dimming and a New CubeSat Mission  
written by James Paul Mason  
has been approved for the Department of Aerospace Engineering Sciences

---

Dr. Thomas Woods

---

Prof. Xinlin Li

---

Prof. Scott Palo

---

Dr. Amir Caspi

---

Prof. Jeffrey Forbes

Date \_\_\_\_\_

The final copy of this thesis has been examined by the signatories, and we find that both the content and the form meet acceptable presentation standards of scholarly work in the above mentioned discipline.

Mason, James Paul (Ph.D., Aerospace Engineering Sciences)

## Solar Eruptive Events:

Coronal Dimming and a New CubeSat Mission

Thesis directed by Dr. Thomas Woods

Often the abstract will be long enough to require more than one page, in which case the macro “\OnePageChapter” should *not* be used.

But this one isn’t, so it should.

## **Dedication**

To my late father, who inspired me from an early age to come this far.

## Acknowledgements

First and foremost, my deepest thanks to Tom Woods. Through the projects he's introduced me to – in solar physics, in sounding rockets, and in small satellites – I've discovered a career path that excites me and that provides continuous opportunities to learn and contribute. Moreover, he's an excellent role model: dedicated and passionate about his work, patient with everyone without seeming to have to try, and exceptionally reliable. All of the above combined has made my time in graduate school likely to be, upon reflection long from now, one of the highlights of my life. Thank you to my committee for guidance and support, most of whom I've been fortunate to work with closely: Xinlin Li, Scott Palo, Amir Caspi, and Jeff Forbes. Finally, I couldn't have struggled through without the support of my peers, especially Allison Youngblood, whose work ethic inspires me and whom I've been extremely lucky to find. Oh, and my dog, Nessie, who requires three walks a day, has turned out to provide the periods of relaxation away from a screen that have aided in my ability to actually comprehend the work I'm doing.

## Contents

### Chapter

<b>1</b>	Introduction	<b>1</b>
<b>2</b>	Relevant Background	<b>3</b>
2.1	Solar Corona	3
2.2	Physics of Solar Eruptive Event Initiation	3
2.3	Space Weather	3
2.4	EUV Emission	3
2.5	Instrument Descriptions	3
<b>3</b>	Mechanisms and Observational Signatures of Coronal Dimming	<b>4</b>
3.1	Mass-loss Dimming	6
3.2	Thermal Dimming	7
3.3	Obscuration Dimming	11
3.4	Wave Dimming	13
3.5	Doppler and Bandpass Dimming	14
3.6	Summary	16
<b>4</b>	Coronal Dimming Case Studies	<b>18</b>
4.1	Observations	18
4.1.1	Simple Dimming Case	18

4.1.2	Complex Dimming Case . . . . .	25
4.2	Flare-Dimming Deconvolution Method . . . . .	32
4.3	Error Propagation . . . . .	35
4.4	Dimming and CME Parameterization Results . . . . .	38
4.4.1	Simple Dimming Case . . . . .	38
4.4.2	Complex Dimming Case . . . . .	38
4.5	Summary . . . . .	38
<b>5</b>	Semi-Statistical Study of Coronal Dimming	<b>39</b>
<b>6</b>	Overview of MinXSS Solar CubeSat	<b>40</b>
<b>7</b>	Thermal Balance Analysis for a CubeSat	<b>41</b>
<b>8</b>	Summary and Future Work	<b>42</b>
<b>Bibliography</b>		<b>43</b>
<b>Appendix</b>		
<b>A</b>	Coronal Dimming Event List and Ancillary Data	<b>46</b>
<b>B</b>	MinXSS CubeSat Mass/Power Tables	<b>48</b>
<b>C</b>	MinXSS Thermal Model Parameter Tables	<b>49</b>

**Tables****Table**

3.1 Dimming mechanisms summary . . . . .	5
4.1 2011 August 4 event statistics . . . . .	28
4.2 EVE precision by emission line . . . . .	36

## Figures

### Figure

3.1	Schematic of mass-loss dimming . . . . .	6
3.2	Schematic of thermal dimming . . . . .	7
3.3	Outflow velocity vs temperature . . . . .	8
3.4	Dimming dependence on temperature in EVE . . . . .	10
3.5	Schematic of obscuration dimming . . . . .	11
3.6	Photoionization cross-sections for H and He . . . . .	12
3.7	Schematic of obscuration dimming . . . . .	13
3.8	Geometry and effect of Doppler dimming . . . . .	15
3.9	Bandpass dimming . . . . .	16
4.1	LASCO coronagraph data for 2010 August 7 event . . . . .	19
4.2	LASCO coronagraph data for 2010 August 7 event . . . . .	20
4.3	AIA contour analysis for 2010 August 7 event . . . . .	21
4.4	AIA before/after images of 2010 August 7 event . . . . .	22
4.5	EVE selected extracted emission lines for 2010 August 7 event . . . . .	24
4.6	LASCO and STEREO coronagraph data for 2011 August 4 event . . . . .	25
4.7	AIA contour analysis for 2011 August 4 event . . . . .	26
4.8	Additional AIA contour analysis for 2011 August 4 event . . . . .	29
4.9	AIA wave analysis for 2011 August 4 event . . . . .	30

4.10 EVE selected extracted emission lines for 2011 August 4 event . . . . .	31
4.11 Flare-dimming deconvolution method example . . . . .	33
4.12 Flare-dimming deconvolution algorithm schematic . . . . .	34

## **Chapter 1**

### **Introduction**

- Solar eruptive events are rapid releases of energy on the Sun that are sometimes directed Earth-ward, making it important to understand them and to forecast their arrival time and magnitude of their impact
- Three basic types of eruptive event: flare, coronal mass ejection, energetic particles this dissertation focuses on the first two
- Some background about solar flare prediction provided in Chapter 2, including my own massive statistical study, which went to print in ApJ my first year of graduate school
- The relationship between coronal mass ejections and the void they leave behind in the solar corona is the primary topic of the dissertation and its discussion spans several chapters.
  - \* Chapter 3 discusses the various physical processes that can lead to an observation that may be interpreted as a dimming, and the amalgamation of related observations that can theoretically be used to identify and isolate each mechanism
  - \* Chapter 4 puts theory to the test in a detailed case study of a single, relatively simple, event. The aforementioned conglomeration of observations were used to determine that this was indeed a simple case with one dimming mechanism dominating the observation; that which theory says should be most strongly related to the associated CME

- \* Chapter 5 expands the study of the relationship between dimming and CMEs by performing an analysis similar to that of the case study but for approximately 30 events. Thus, a tentative statistical correlation between dimming and CME parameterizations could be derived.
- The topic of solar flares is picked up again briefly in the science motivation for the solar CubeSat MinXSS. An overview of the mission is the topic of Chapter 6, which includes science motivation, system overview, and lessons learned.
- Chapter 7 delves deeper into the CubeSat engineering with a detailed thermal balance test and model analysis, culminating in the (likely) first ever tuned CubeSat thermal model that has been validated by dedicated testing and on-orbit measurements.
- Chapter 8 provides a summary of deliverables and results, and lays out plans for future work. The latter will be the first steps in my post-doc that has already been secured through my first grant being funded as well as SDO/EVE and MinXSS extended mission funding.

## **Chapter 2**

### **Relevant Background**

**2.1 Solar Corona**

**2.2 Physics of Solar Eruptive Event Initiation**

**2.3 Space Weather**

**2.4 EUV Emission**

**2.5 Instrument Descriptions**

## Chapter 3

### Mechanisms and Observational Signatures of Coronal Dimming

This chapter details the physics of coronal dimming and the observational signatures that result. There are theoretically many physical processes that can lead to an uncareful observer identifying "dimming", which may have little to do with a coronal mass ejection (CME). Traditionally, the term "coronal dimming" has been assumed to refer to the void left in the corona after a CME departs. This is one cause of a transient hole in the corona and is of the greatest concern to space weather forecasters. However, changing temperatures (common during solar eruptive events) cause ionization fraction shifting, resulting in some emissions dimming while others brighten. Additionally, dark material (e.g., a filament) can pass between a bright region (e.g., flaring loops) and the observer, causing a transient dip in emission. Third, solar eruptive events sometimes have associated waves that propagate across the solar disk. These waves are observed as narrow bright fronts with a trailing dark region. The trailing dark region is another way to achieve a transient dimming of emission. Next, there are two ways that Doppler effects can cause transient dips in emission. The first is called Doppler dimming and results from fast moving plasma being sufficiently Doppler-shifted to reduce resonant fluorescence from the solar emission line sources; a phenomenon which is independent of the observation angle. The second occurs if eruptive plasma is moving fast enough in the line-of-sight to shift its emissions outside the bandpass of an observing instrument, which we have named "bandpass dimming". The physics and instrumental identifiers for each of these types of theoretically observable dimming are summarized in Table 3.1 and are discussed in detail in the sections that follow.

Table 3.1: Summary of physical processes that can manifest as observed dimming

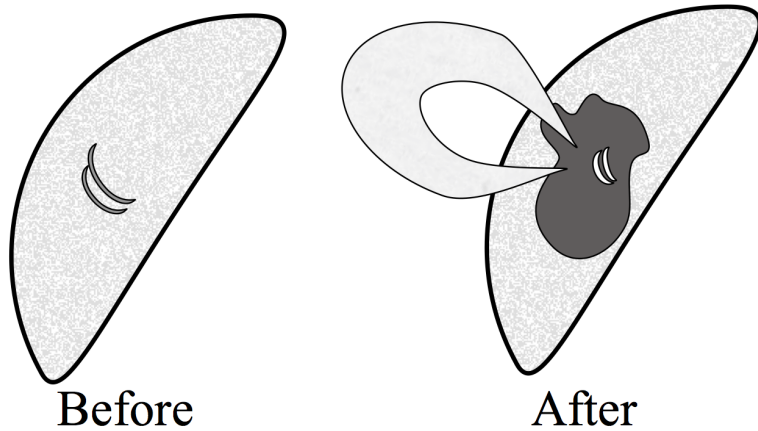
Short Name	Physical Process	EVE Observational Identifiers	AIA Observational Identifiers
Mass loss (Fig. 3.1)	Ejection of emitting plasma from corona	Simultaneous intensity decrease in multiple coronal emission lines, with percentage decrease indicative of percentage mass lost	Area over and near the erupting active region (AR) darkens
Thermal (Fig. 3.2)	Heating raises ionization states (e.g., a fraction of Fe IX becomes Fe X); cooling does the opposite	Heating: Emission loss in lines with lower peak formation temperatures and near simultaneous emission gain in lines with higher peak formation temperatures; vice versa for cooling	Heating: Area near AR darkens in channels with lower peak formation temperature and near simultaneous brightening in channels with higher peak formation temperatures; vice versa for cooling
Obscuration (Fig. 3.5)	Dim feature (e.g., filament material) moves into line-of-sight over a bright feature (e.g., flare arcade)	Drop of emission lines proportional to their absorption cross section in the obscuring material	Direct observation of this obscuration process
Wave (Fig. 3.7)	Wave disturbance propagates globally, causing compression/rarefaction of plasma as wave passes by	No effects have been identified	Direct observation of this wave process, especially apparent with difference movies
Doppler (Fig. 3.8)	Fast moving plasma Doppler shifts away from resonant fluorescence with solar emission lines	Doppler wavelength shift of emission lines and change in intensity, possibly also observed as line broadening	Change in intensity of moving plasma as its velocity changes
Bandpass (Fig. 3.9)	Emissions from fast moving plasma have Doppler wavelength shift	Emission line shifts in wavelength or has broadening	Doppler shift convolves with band-pass sensitivity to cause apparent reduction in emission

### 3.1 Mass-loss Dimming

The physical process in mass-loss dimming is the ejection of emitting plasma (see Figure 3.1; Harrison and Lyons 2000; Harra and Sterling 2001). It can be a CME or a failed ejection, the latter of which still manifests locally as a mass-loss dimming, but does not result in the appearance of a CME in coronagraph data and may not appear in a disk-integrated spectrograph like EVE. The physics model is the standard CME initiation discussed in Section ???. However, where most discussions will then follow the CME as it transitions to an interplanetary CME, in mass-loss dimming we are instead interested in the details of the void left behind in the corona. The mass of an average CME and a typical active region are of the same order of magnitude:  $10^{15}$  g, meaning that a departing CME can "blow out" a large part of the active region with it (Aschwanden et al., 2009). This is the physical process assumed to be the main contributor to observed dimming in many recent studies (Sterling and Hudson, 1997; Reinard and Biesecker, 2008, 2009; Aschwanden et al., 2009). Harrison et al. (2003) showed that dimmings can account for a large percentage of CME mass. Thus, mass-loss dimming is very relevant for the space weather community.

Observationally, mass-loss dimming appears in EVE as multiple emission lines dropping

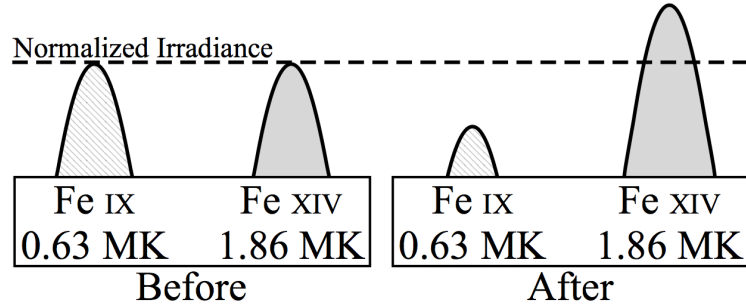
Figure 3.1: Schematic depicting the process of mass-loss dimming. Prior to the eruption (left), coronal loops are relatively quiescent. During and after the eruption (right), the loops are brighter and reconfigured, a CME is ejected, and a void forms in the coronal plasma.



nearly simultaneously. In the case of a failed ejection, the dimming area and the ejected material are likely to maintain a total emission that is close enough to constant that it will not be apparent in EVE data. For space weather, this is of little concern since CMEs have far greater geoeffectiveness than short-lived holes in the corona of small spatial extent. However, AIA data allow the identification of mass-loss dimming even if the event is a failed ejection. In either case, mass-loss dimming appears in AIA as a relatively compact area near an active region becoming darker, sometimes with a dark cloud visibly moving off-disk. Assuming the dimmings in Reinard and Biesecker (2008) to all be due to mass loss, the timescale of the process is 3 - 12 hr and rarely persists longer than a day. Additional observations from the Hinode spacecraft have confirmed density decreases with accompanying outflows (Attrill et al., 2010; Harra et al., 2010; Tian et al., 2012).

### 3.2 Thermal Dimming

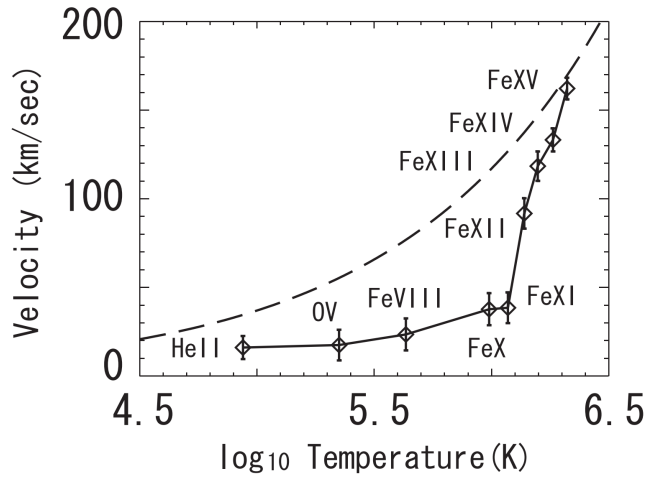
Figure 3.2: Schematic depicting the observational difference between dimming and non-dimming emission lines. Relative to a pre-eruption time (left), the Fe IX emission drops while the Fe XIV emission increases (right) due to heating of the plasma and redistribution of ionization states.



Temperature evolution of emission lines is only interpreted as observed dimming if one is not careful to observe co-spatial emission lines at different peak formation temperatures. As plasma is heated or cooled, the ionization fraction changes, necessarily causing the emission intensity to change (Figure 3.2). For example, heating causes some Fe IX to become Fe X and thus, in the

absence of competing physical processes, 171 Å emission drops while 177 Å rises. This pattern was identified observationally in Figure 6 of Woods et al. (2011) using SDO/EVE data, Robbrecht and Wang (2010) using STEREO/EUVI, and Jin et al. (2009) and Imada et al. (2007) with Hinode/EIS. It can also be observed in the standard composite (multi-wavelength) movies produced by the AIA team; indeed, this is one of the prime purposes for the composites. The initiation time and duration of temperature evolution tends to be quite similar to mass-loss dimming, as they are typically both responses to the rapid release of magnetic field energy in active regions and require several hours of recovery time. Thus, thermal processes could be mistaken for mass loss if only a single spectral line was observed. Ideally, unblended emission lines from an entire coronal ionization sequence (e.g., Fe I to Fe XVIII) could be used to mitigate this convolution of dimming observations. However, as we will show in Section 4.3, it may be sufficient to have observations of two sufficiently separated ionizations states to differentiate between thermal evolution and mass-loss dimming. This is due, in part, to the fact that hotter lines (e.g., Fe XV and above) are primarily emitted from confined loops near the flare and are thus not strongly impacted by mass-loss dimming.

Figure 3.3: Outflow velocity vs emission line peak formation temperature for a dimming region near a plage. Adapted from Imada et al. (2007).



Multi-wavelength Doppler studies have shown that while all (measured) emission lines become

blue-shifted (indicating an outflow), the magnitude of the shift is strongly directly proportional to the lines peak formation temperature (Imada et al., 2007; Jin et al., 2009). Figure 3.3 shows this dependence for a plage region with a dimming during an X-class flare. Part of the explanation for this is that as a population of ions is accelerated outward as part of the CME, it is simultaneously experiencing heating as part of the eruptive process. This causes the ionization fraction to shift upward to the point where there may be little low ionization states left e.g., Fe IX. Tracking a single ion, one would see the same nuclei accelerating outward while having electrons stripped away. This explains why lower ionization states seem to have relatively little velocity. Additionally, Fe IX 171 Å emission can be depressed further after open magnetic field lines from the departing CME close down and cause another bout of heating; causing e.g., Fe IX to become Fe X and beyond, which propagates outward as a "heat wave dimming" (Robbrecht and Wang, 2010). However, Mason et al. (2014) found that the onset time, slope, and duration of dimming are comparable in SDO/AIA 171 Å and 193 Å<sup>1</sup> and in SDO/EVE 171Å and 195 Å (described in Chapter 4) It should also be noted that EUV images tend to provide higher contrast for dimming in Fe XII 195 Å than Fe IX 171 Å. This is because there is much less Fe XII in the quiescent corona than Fe IX. Therefore, the background in 171 Å images is much brighter, making dimming (which are typically less than a 5% reduction of global emission) more difficult to identify. Nevertheless, we find that for global emission (i.e., irradiance) 171 Å shows stronger dimming than 195 Åas shown in 3.4.

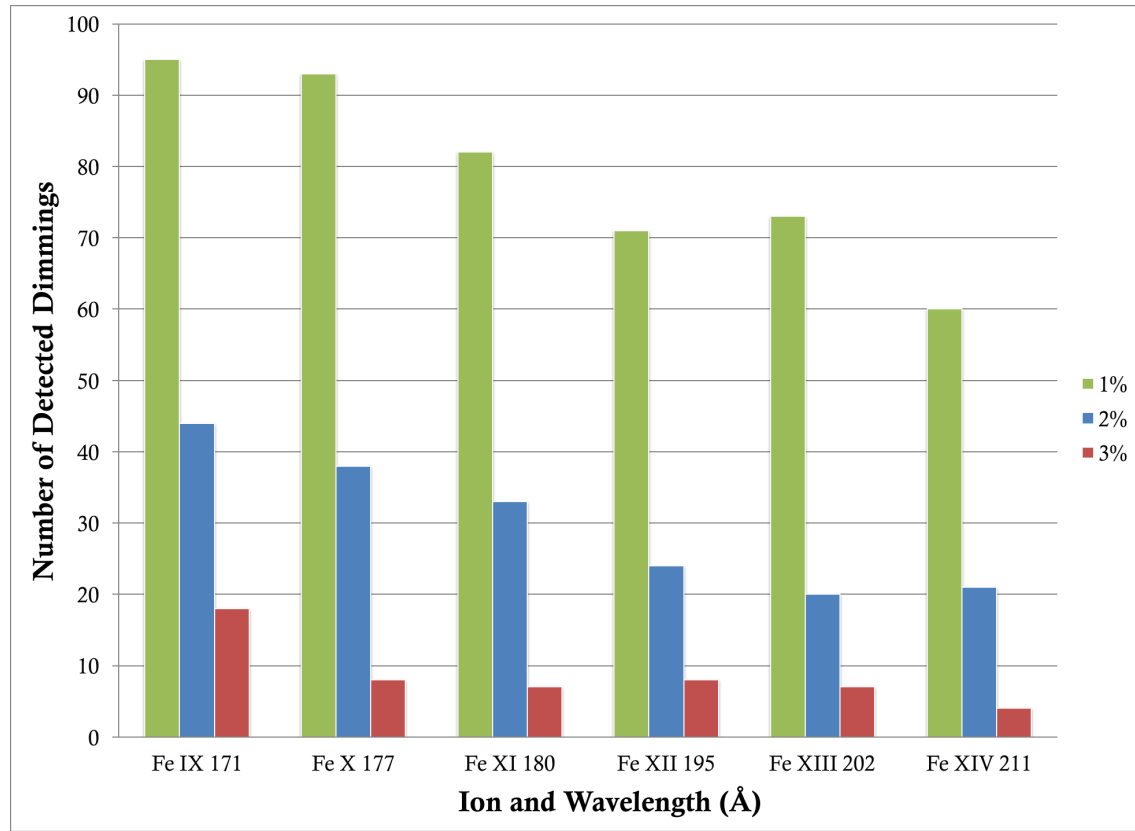
It is important to note that, in general, the magnitude of total observed dimming in a given line in EVE spectra is inversely proportional to its peak formation temperature, which can be inferred from Figure 3.4. This figure was generated using a simple algorithm that searched all EVE/MEGS-A data for relative irradiance decreases greater than a specified threshold (1%, 2%, 3%) of flares exceeding GOES X-ray class of C1. The window of time searched was bounded by the GOES event start time and the sooner of either 4 hours after the start time or the next GOES event start time. This algorithm was applied to all EVE data from mission start (2010 May 1) to the failure of the MEGS-A instrument ( 2014 April 30). MEGS-A takes the measurements of all

---

<sup>1</sup> Note that the SDO/AIA 193 Å band encompasses 195 Å

wavelengths studied here. Figure 3.4 shows that the number of dimmings dramatically decreases as the magnitude threshold is increased, and decreases slightly with higher peak formation temperature. This latter effect is partially due to flare heating adding emission in the higher temperature, higher ionization state, lines that partially offsets the mass-loss dimming. Additionally, these trends indicate that at sufficiently high peak formation temperature, no dimming may be observed at all, even at the lowest detection threshold, which is consistent with the hotter lines being restricted to the confined flare loops and hence experiencing no mass loss. In other words, the higher the peak formation temperature, the greater the relative contribution of more confined loops to the measured emission.

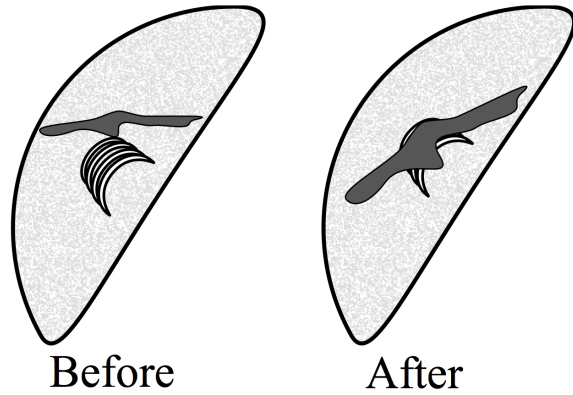
Figure 3.4: Number of identified dimmings in EVE for six spectral lines using different percentage dimming depths as the threshold for a detection. There were 302 flares ( $\geq$  M1.0 GOES class) used to trigger an automated search for dimming in EVE. Note the decrease in detections with increasing ionization state (i.e. peak formation temperature).



An instrument with spatial resolution like AIA can be used to isolate the confined flaring loops and create a time series of just the dimming region, and this is a procedure carried out in Chapter 4. AIA too has its own limitations; relevant in this case is the relatively lower spectral resolution that blends together emission from several ionization states of Fe. With EVE and AIA combined, it is possible to analyze thermal dimming but the ideal instrument for fully characterizing this phenomenon would be a high-resolution hyperspectral imager in the EUV.

### 3.3 Obscuration Dimming

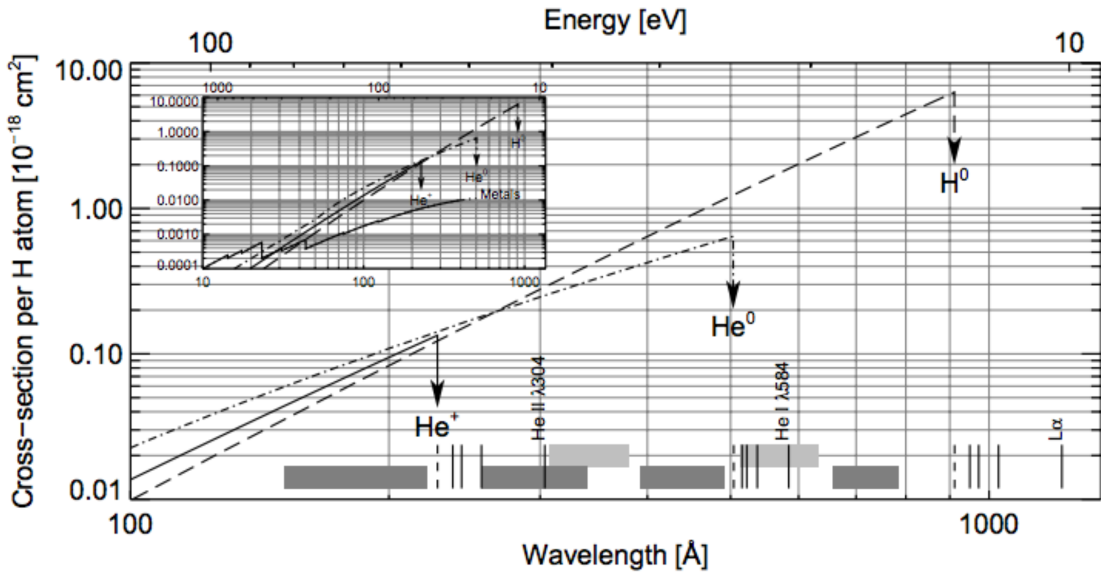
Figure 3.5: Schematic depicting the process of obscuration dimming. A filament previously obscuring only the quiet Sun (left) expands and moves in front of a flare arcade (right). This results in a decreased observed emission from the flare arcade in wavelengths where the filament is optically thick.



The physical process that results in apparent dimming here is material that is dark in a particular wavelength (e.g., a filament) moving between bright material (e.g., flare arcade) and the observer (Figure 3.5). In optically thick wavelengths, the dark plasma absorbs some of the bright emission, resulting in an apparent decrease in emission. The slow draining of plasma back to the corona can obscure underlying emission for hours, and absorption can be observed in both coronal and chromospheric lines (e.g., Gilbert et al. 2013). Although obscuration dimmings can exhibit time and spatial scales comparable to the more short-lived mass-loss dimmings, it is fairly straightforward to identify absorption signatures in the EUV images. It may also be possible to

identify this phenomenon with EVE using the He II 256 Å and 304 Å chromospheric emission lines and knowledge of the absorption cross-section through filamentary plasma. Figure 3.6 shows the photoionization cross-sections of the dominant species in the solar corona. Hydrogen and helium contribute an order-of-magnitude more absorption than metals<sup>2</sup>, and thus the effect of metals can be ignored. The cross-sections are quite steep in the wavelength range of interest here (roughly 150-310 Å). This means that approximately twice as much He II 256 Å than He II 304 Å emission will come through a filament. Furthermore, the mass-loss dimming sensitive lines (e.g., Fe IX 171 Å and 195 Å) will be less affected by this obscuration, but a 1% effect would be sufficient to cause a "false" detection. It may be possible to identify obscuration dimming with EVE's 256 Å and 304 Å measurements and determine that an obscuration dimming has occurred. However, further analysis of this type of dimming is required before any conclusions can be drawn.

Figure 3.6: Photoionization cross-sections for He I (dot-dashed line), He II (solid line), and H (dashed line) per hydrogen atom. The inset shows a wider wavelength range of the same data but with metals shown for comparison. The dashed vertical bars at the bottom indicate the edges of respective continua. The grey regions at the bottom are not pertinent here as they correspond to specifics of the SOHO/CDS instrument. Adapted from Andretta et al. (2003).

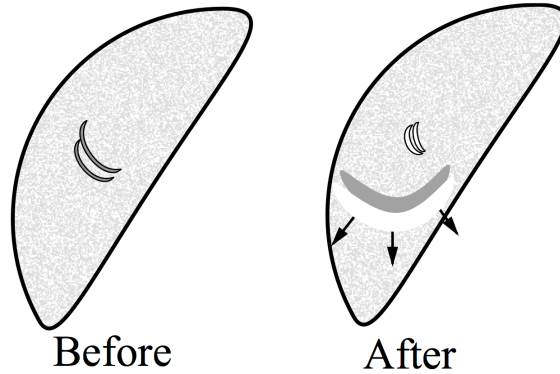


<sup>2</sup> "Metals" in the astrophysical sense

### 3.4 Wave Dimming

The debate about the physics of coronal EUV waves continues (e.g., Zhukov and Auchère 2004; Muhr et al. 2011; Liu and Ofman 2014) but one of the simplest explanations of the observations is that plasma is compressed as a longitudinal wave passes through the medium. Traveling (i.e., not static) rarefactions are sometimes observed following the compression (Muhr et al., 2011), the compressed regions having higher densities resulting in increased emission, and vice versa (Figure 3.7). Alternatively, some models suggest that the observed phenomenon is not a wave at all, but rather the impact of the CME departing on the global magnetic field (Chen et al., 2002, 2005). Regardless of the physical process responsible, the observation is the same. The EUV waves emanating from an eruption can be seen to cause dimmings and brightenings elsewhere in the solar EUV images, often very far from the original eruption site, particularly near other active regions. We refer to these dimmings that are non-local to the erupting site as sympathetic dimmings (Schrijver and Higgins, 2015). This is quite likely to occur if a distant active region has significant potential energy stored when the disturbance reaches it – the wave propagating across the magnetic field lines acts as a catalyst.

Figure 3.7: Similar to Figure 3.5, but depicting the process of wave dimming. After an eruptive event, a wave propagates and expands through the corona. The compressed plasma of the wavefront results in enhanced emission, while the rarefied trailing region is dimmed.



It is important to distinguish between the wave-caused dimmings and other causes of remote

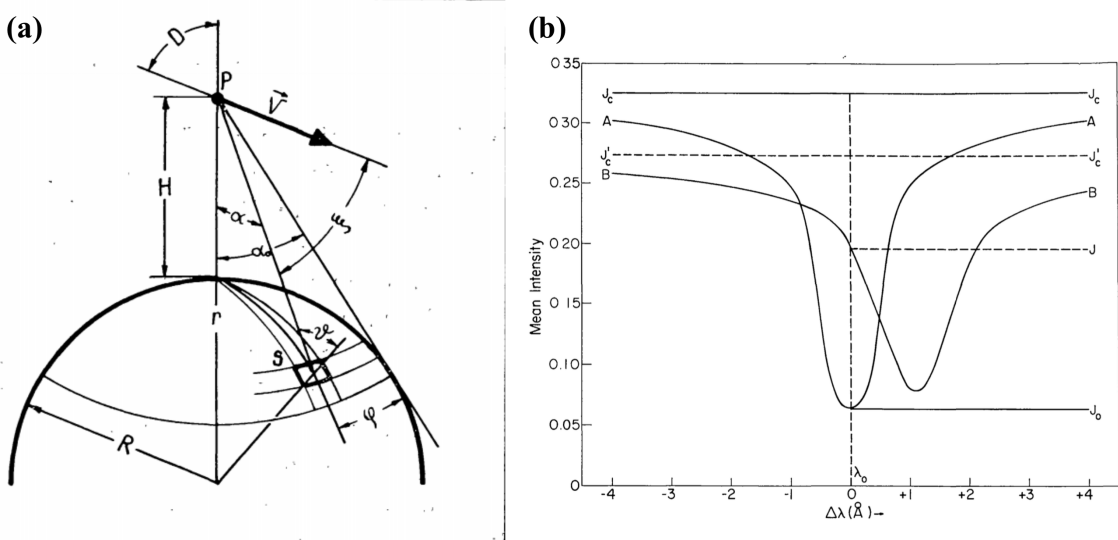
dimming, such as large-scale disappearing loops that are visible in soft X-ray images but only have visible EUV changes at their footpoints (Pohjolainen et al., 2005). EUV wave dimmings are unlikely to be easily identified in full-disk spatially-integrated instruments like EVE because the enhanced emission nearly cancels out the dimmed emission when summed.

### 3.5 Doppler and Bandpass Dimming

Two additional processes can theoretically lead to the observation of dimming in a limited wavelength range and both result from Doppler effects. The first has been given the name "Doppler dimming". In this type of dimming, resonant fluorescence of a high-velocity, remote cloud of plasma (e.g., CME) by a source population (solar emission lines) can decrease as the resultant Doppler shift becomes sufficiently large (see Figure 3.8; Hyder and Lites 1970). Here, Doppler takes effect due to the relative velocity between the source (the Sun) and the scattering medium (the CME) and is thus independent of observer angle. This phenomenon has been known for decades for cometary emissions (Swings, 1941; Greenstein, 1958) and has been documented in chromospheric lines associated with eruptions (Labrosse and Mcglinchey, 2012) as well as in coronal lines such as O VI for polar coronal hole outflows (Giordano et al., 2000). However, the majority of EUV emission lines in the corona are collisionally dominated i.e. not resonantly excited, and will not exhibit this effect. Furthermore, the dimming region is the CME itself, which is likely to be outside the field of view of EUV instruments observing the solar disk. Therefore, it is possible to diagnose this type of dimming when it is pronounced in resonantly excited lines but does not manifest in the lines of interest studied herein.

The second type of dimming that results from a Doppler effect is one we call "bandpass dimming". This physical process is tied to the observers location similarly to obscuration dimming (see Section 3.5). Mass ejected toward the observer will have emissions that are necessarily blue-shifted. If the velocity is high enough, it can shift emission lines outside of an imager's bandpass, causing an apparent dimming in the data. Most imagers use filters that tend to have bandpasses on the order of nanometers but can have sharp edges (Figure 3.9). CMEs typically have speeds

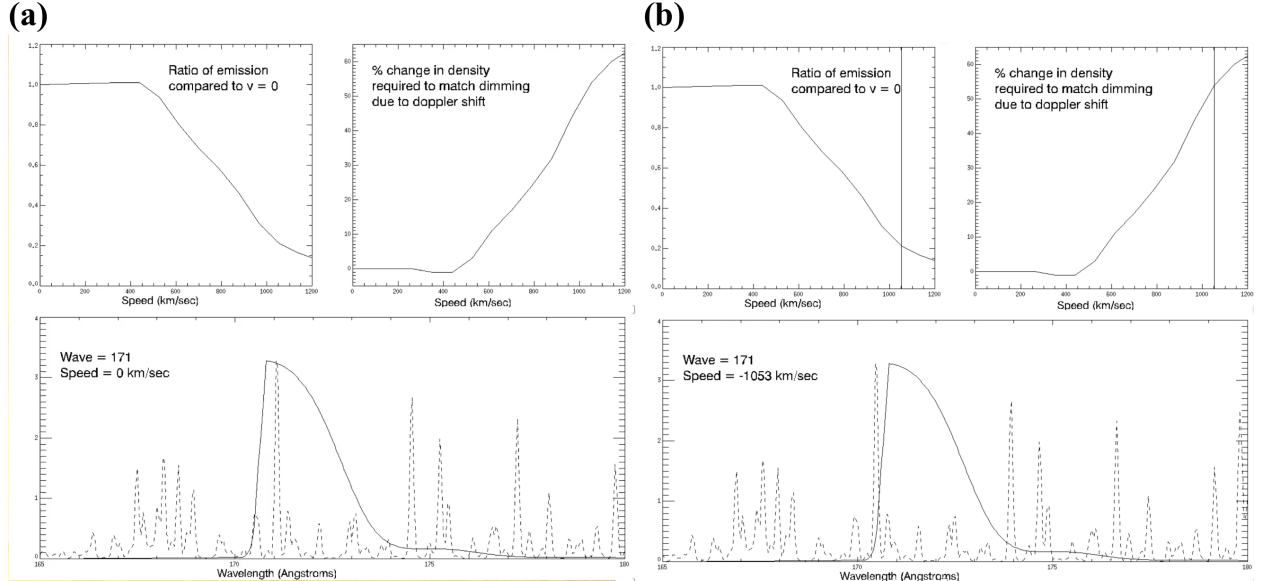
Figure 3.8: (a) Geometry of Doppler dimming. The large circle at the bottom represents the Sun, the point P represents the position of mass that has erupted e.g., a CME. The vector V is the velocity of the CME. The square patch on the Sun represents an area of source emission. Adapted from Rompolt (1967). (b) The H $\alpha$  profiles seen by (A) a stationary observer at a height of 5600 km above the photosphere; and (B) an observer at a height of 30,000 km moving radially outward at 75 km s $^{-1}$ . The mean intensity (as seen by the scattering medium) is measured in units of the intensity of the nearby continuum at the center of the disk. It can be seen that the Doppler shift also causes an intensity decrease. Adapted from Hyder and Lites (1970).



ranging from a few hundred to a couple thousand km s $^{-1}$ . However, a CME only accounts for a small fraction of the total emission from the solar disk. As noted in Hudson et al. (2011), these Doppler shifts tend to be on the order of picometers. Additionally, a CME moving fast enough to shift emission outside the bandpass would be outside the field-of-view of the instrument in a very short time. Thus, this type of apparent dimming is not expected in EUV images, but we include it for completeness and note that this may be a consideration for future instrumentation.

In a spectrograph like EVE, the Doppler shifts would instead simply cause a wavelength shift of the emission line from the ejected material, which is how Hudson et al. (2011) performed their analysis. When this Doppler-shifted emission is convolved with the relatively static plasma remaining on the Sun, a small Doppler shift from the ejected material manifests as line-broadening in the integrated irradiance while a large shift would result in a line splitting. It should be noted

Figure 3.9: (a) and (b) are snapshots from a movie produced by Barbara Thompson. (a) Bottom: The dashed line shows a modeled solar spectrum and the solid line shows the bandpass for AIA’s 171 Å. Top left: The ratio of emission relative to plasma with no line-of-sight velocity as a function of velocity. Top right: The amount of density decrease (in %) that would be required to achieve the same amount of dimming as bandpass dimming at each velocity. (b) Same as (a) but at a velocity of  $1053 \text{ km s}^{-1}$ .



that the EVE extracted lines data product applies a static mask to the spectra so a sufficiently large Doppler shift could cause an apparent dimming in this product. Again, the observed shifts are far too small to impact the EVE data analysis.

### 3.6 Summary

The physics for most of these types of dimming is relatively simple and well-understood, with the exception of global waves. Mass-loss dimming is simply the direct result of a CME removing a significant quantity of emitting material from the solar corona. This dimming is not immediately lost as the CME pulls away because the post-eruption relaxation period is nonzero and it can take several hours for the quiescent Sun to replace the lost plasma from the surrounding corona and transition region. Instrumentally, even though EUV measurements select specific temperature ranges, mass-estimates based on them appear consistent with white-light coronagraph derived

masses (Aschwanden et al., 2009).

Thermal dimming is a major concern in nearly all of the citations above for its potential to interfere with mass-loss dimming and the resultant estimated CME masses. The physics here is also simple: eruptive events result in various forms of heating (see Section ??) that shift upward the ionization fraction of dominant EUV emitters (e.g., Fe). Instrumentally, this effect can be compensated for by measuring emission lines from multiple ionization states of the same ion (e.g., Fe IX-XV).

Obscuration dimming physics are also simple, essentially a result of Beer's law, as light passes through a medium with nonzero opacity. Instrumentally, this is easily identified with imagers and we believe it may be possible to identify with a spectrograph, provided some chromospheric helium emission lines are measured (e.g., 256 Å and/or 304 Å).

The physics of global waves is highly contested but the observations are well established. For a disk-integrating spectrograph like EVE, which is the primary source of data analysis herein, we believe that wave dimming will be negated by wave brightening. Indeed, to our knowledge, no observations of waves have been made with EVE.

Doppler dimming physics are well understood and long standing. A CME may fluoresce due to stimulation from the Sun, but the wavelengths will be Doppler shifted according to the relative velocity of the CME from the Sun. This shift reduces the efficacy of the stimulation, resulting in less fluorescence. However, the dimming region in this case is the CME itself, which is likely to be outside the field of view of instruments like AIA and EVE. Additionally, the emission lines of interest in this study are collisionally dominated. Thus Doppler dimming is an interesting phenomenon but is not expected to dramatically impact analyses of the other types of dimming.

The physics of bandpass dimming is simple Doppler shifting of an emitting plasma. Potential dimming in this case is primarily an instrumental effect, as the Doppler shift could push important emission lines outside the instruments bandpass or data processing line-selection masks. However, studies have shown that the actual Doppler shifts are orders of magnitude too small to cause this type of dimming.

## **Chapter 4**

### **Coronal Dimming Case Studies**

This chapter focuses on the detailed analysis of two coronal dimming events. One was selected for its relative simplicity, involving only mass-loss dimming and thermal dimming, while the other was selected for its complexity, involving nearly all of the types of dimming as described in Chapter 3. The EUV irradiance and imaging observations of these events as well as the related coronagraph observations are first described in Section 4.1. A new method for deconvolving flare emission from dimming irradiance measurements is developed in Section 4.2 while Section 4.3 contains the associated error propagation. Finally, Section 4.4 provides analyses and results of these two coronal dimming events. We find that the new deconvolution method for irradiance successfully matches the dimming profile extracted from the spatially-isolated dimming as obtained from EUV image time series. Thus, we show that it is possible to accurately characterize dimming in a localized area even with no spatial resolution.

#### **4.1 Observations**

##### **4.1.1 Simple Dimming Case**

This event occurred on 2010 August 7 at approximately 18:24 UT. The eruptive event consisted of an M1.0 flare, dimming in the region around the flare, and a coronal mass ejection (CME). Other active regions were also on disk but did not have any significant sympathetic responses. Mass-loss and thermal dimming were found to be important, while the other type of dimming (see Chapter 3) were negligible.

### Coronagraph Observations

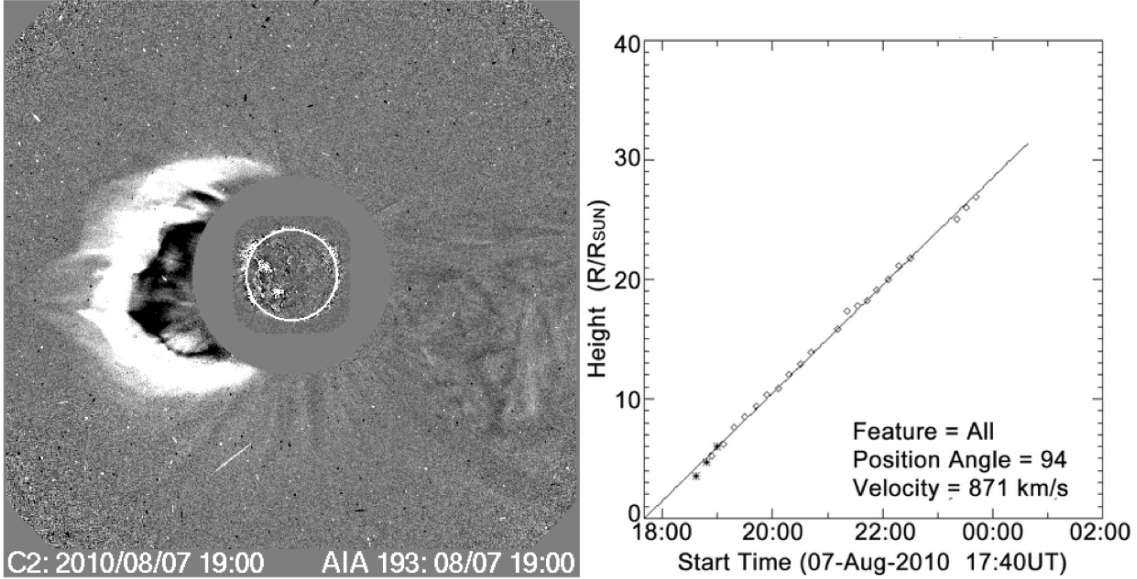


Figure 4.1: CME event at 19:00 on 2010 August 7. Left: difference image from LASCO C2 and AIA 193 Å channel. Right: CME height versus time shows nearly linear velocity of  $871 \text{ km s}^{-1}$ . Figure adapted from CDAW CME Catalog, courtesy of S. Yashiro and N. Gopalswamy.

The Coordinated Data Analysis Workshops (CDAW) LASCO CME catalog (herein referred to simply as the CDAW catalog) is an extensive database of all CMEs observed by the SOHO/LASCO coronagraphs with related quantities such as date, time, computed velocity, and sometimes mass (Gopalswamy et al., 2009). The CDAW catalog has seven CME events listed for 2010 August 7. All but two of them occur prior to the M1.0 flare at 18:24 UT that is of primary interest for the present study. The CME shown in Figure 4.1 is flagged as a halo event with a time of 18:36 UT in CDAW, while the next event occurred with a central position angle of  $116^\circ$  at 22:24 UT. The timing and location of the flare and associated dimming region suggest that the halo CME is associated with the dimming. The plane-of-sky velocity estimate for this CME is  $871 \text{ km s}^{-1}$  as indicated in Figure 4.1. No mass is listed for this CME in CDAW, but using LASCO and STEREO data and the techniques outlined in Colaninno and Vourlidas (2009), a mass of  $6.4 \times 10^{15} \text{ g}$  was computed for this CME event (A. Vourlidas 2014, private communication). A true space velocity was also computed as  $850 \text{ km s}^{-1}$  at  $9 \text{ R}_{\odot}$  with a deceleration of  $6.84 \text{ m s}^{-2}$  (Figure 4.2). Based on these

estimates for mass and velocity, this CME is considered be of modest size.

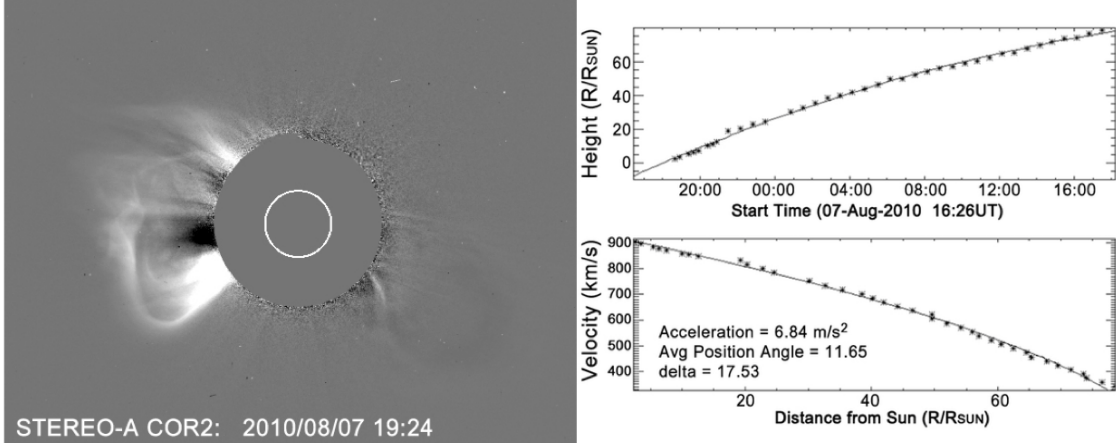


Figure 4.2: Left: STEREO-A COR2 difference image at 19:24 UT. Right: CME height vs. time calculated from STEREO and shows a deceleration of  $6.84 \text{ m s}^{-2}$ . Figure courtesy of Barbara Thompson.

**SDO/AIA EUV Image Observations** The relative simplicity of this event is why it was chosen for a case study. The observations in AIA do not suggest that obscuration, waves, or Doppler shift contributed to the observed dimming. The area in the red contour of Figure 4.3 was selected manually (by eye) to represent the region of mass loss, and its light curve shows clear dimming in 193 Å and 171 Å. In fact, the dimming from this region accounts for nearly all of the observed dimming throughout the entire event. This contour was selected after several iterations that indicated slight deviations in the contour had minimal impact on the light curve, as long as the dark region was fully encompassed. In other words, the result is fairly insensitive to the precise contour selection. The other contours were also selected manually to isolate regions of potential dimming e.g., as a sympathetic response from the solar eruptive event of interest. The exception is the magenta contour surrounding the flare loops that brightens dramatically but does not ever dim.

The He II 304 Å light curves are included to provide a contrast to the dimming effects seen in the coronal Fe lines. This He II wavelength is generated primarily in the chromosphere and transition region, as opposed to the coronal source of the other wavelengths. Mass loss occurs

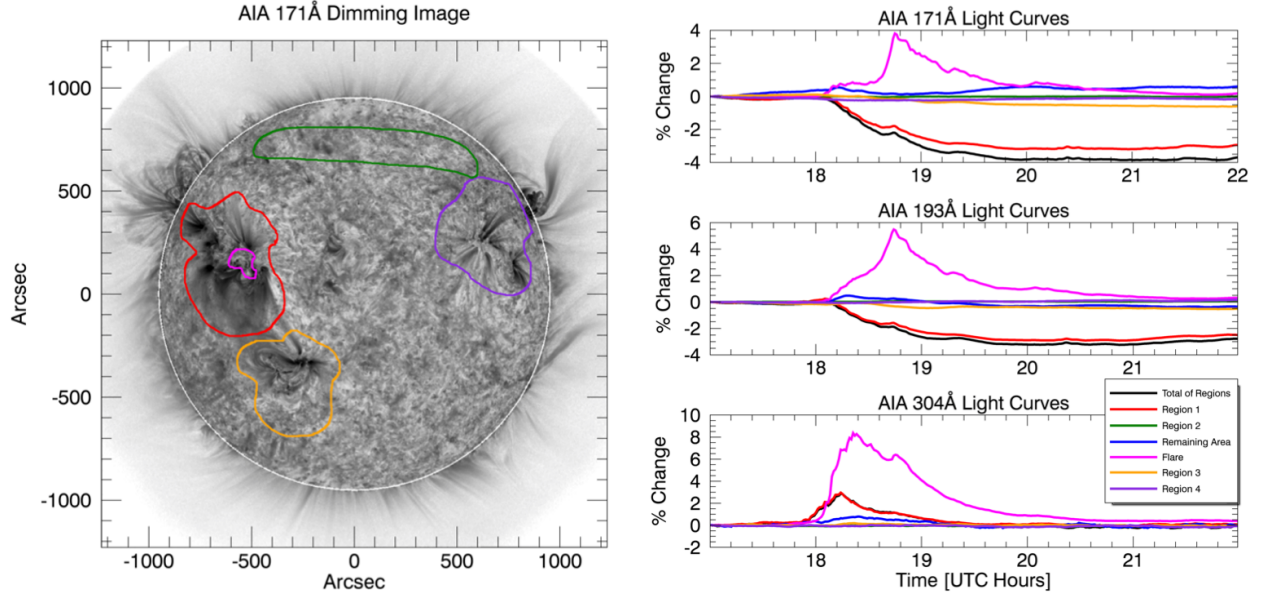


Figure 4.3: AIA results for the M1.0 Flare on 2010 August 7. Images improved by using point spread function to compensate for instrument "blurring" of light. Left: AIA 171 Å channel difference image with subjectively selected region contours overlaid. The red contour outlines what is thought to be the region of mass loss. The orange and purple contours outline other active regions on the disk, which have the potential to have sympathetic dimming. The green contour outlines a filament, which also has the potential to sympathetically dim based on its behavior during the M flare on 2010 August 5. The magenta contour isolates the flaring coronal loops. The white line around the solar limb is an artifact of the solarsoft derotation method. Right three plots: light curves of AIA 171 Å, 193 Å, and 304 Å channels for the color-corresponding contours on the AIA image. The blue line is the light curve for all on-disk area not enclosed by a contour. The black line is the sum of all contoured regions and acts as a proxy for total dimming. All percent changes are calculated from the bands value at 17:00 UT, prior to the flare. The transition region He 304 Å emission does not show dimming; both corona Fe emissions (171 Å and 193 Å) show dimming.

primarily in the corona, as the term coronal mass ejection suggests. This is reflected in the lack of dimming observed in the non-coronal He II 304 Å emission line.

Thermal dimming may play a role in this event but may be difficult to quantify using only AIA because the relatively wide spectral bands of AIA channels mean many emission lines and any continua are blended together, which makes specifying a well-defined temperature difficult. Nevertheless, some indication of temperature is given by AIA and images that composite multiple wavelengths can aid in this analysis. Figure 4.4 shows AIA composite images (211 & 193 & 171 Å) before the solar eruptive event and during the dimming. All of these bands correspond primarily to

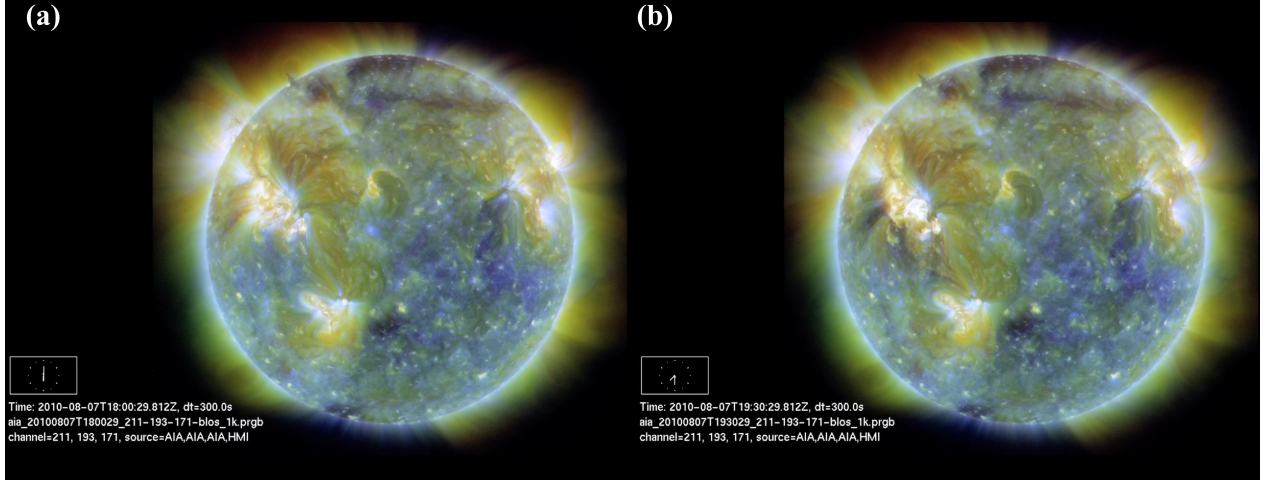


Figure 4.4: AIA composite images (a) prior to solar eruptive event and (b) during deep dimming. In these images, purple is 211 Å, brownish-gold is 193 Å, and yellow is 171 Å. These static images show dimming in the region as outlined in Figure 4.3, though the change much more dramatic and obvious when viewed as a movie.

the corona and transition region. If an area is dark, that means that there is little emission in all three of these wavelengths. Since these three bands span at least temperatures from 0.6-1.86 MK, that is indicative of mass loss. Even in areas of extreme heating, e.g., confined flare loops, it can be seen that emission is strong in all three of these bands resulting in the composite being white. Thus, it's unlikely that a region in these composite would become dark purely from a temperature change. EVE is less sensitive than AIA to blending in temperature space due to its higher spectral resolution and plethora of emission lines from Fe at different ionization states. A future study using the differential emission measure techniques of Caspi et al. (2014) to study the temperature evolution could help to quantify this effect.

**SDO/EVE EUV Irradiance Observations** Figure 4.5 shows a trend that is consistent with the findings from Figure 3.4 -that an ions peak formation temperature is inversely proportional to magnitude of dimming. The transition from an ionization state that shows dimming to ones that only show brightening occurs at Fe XIV 211 Å, which itself shows dimming in some events but not others. The transition for where the Fe emission shows dimming is different for different solar eruptive events. For example, the Fe XVI 335 Å emission has shown dimming for larger CME

events (Woods et al., 2011). Herein, we will refer to Fe IX 171 Å through Fe XIV 211 Å as dimming lines for the 2010 August 7 event, and Fe XIV 211 Å through Fe XXIV 192 Å as nondimming lines (note that 211 Å is included in both descriptions to reflect its ambiguity).

It is also interesting to note in Figure 4.5 that the onset of dimming in the dimming lines is nearly simultaneous. The gradual-phase flare peak is delayed in lower ionizations of Fe, which is due to a cooling effect. The primary source of energy release in a flare is near the point of magnetic reconnection, typically far above the footpoints of the magnetic loops involved, in the corona. Some of the energy goes into the acceleration of particles downward. When these particles impact the denser chromosphere, they cause the heating and chromospheric evaporation. As that thermal plasma enters the corona it cools (Fletcher et al., 2011), and highly ionized Fe gains electrons. Thus, the peak is later for lower ionization states as seen in Figure 4.5. The Fe IX 171 Å irradiance, in particular, shows the competing effects of this gradual phase flare peak and coronal dimming. Images with spatial resolution can isolate the flaring region responsible for this peak, as is shown with the magenta contour in Figure 4.3. Alternatively, we have developed a method for isolating and removing this peak in dimming lines with the spatially-integrated irradiance from EVE, which will be detailed in Section 4.2.

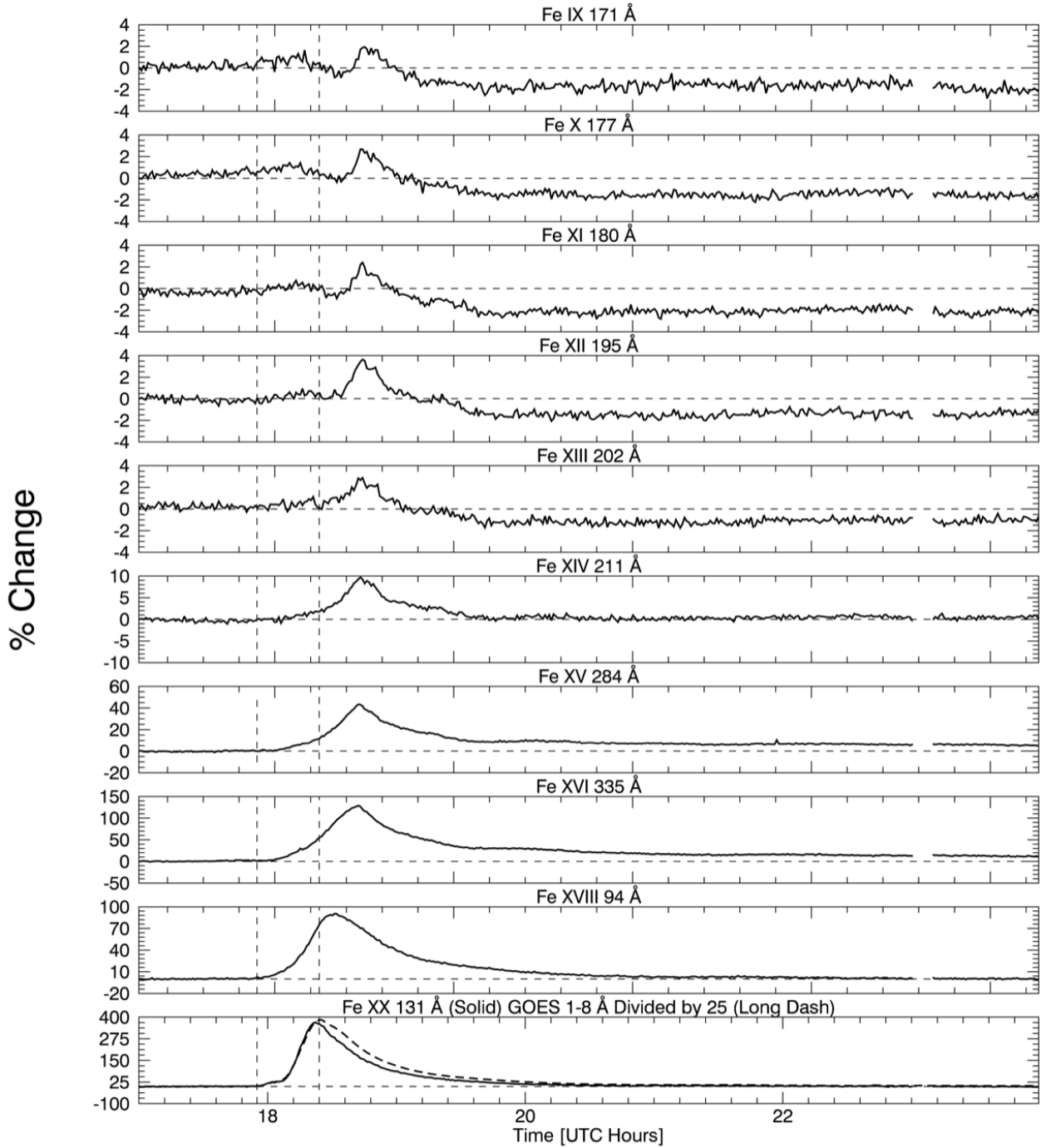


Figure 4.5: One minute average EVE light curves of the 2010 August 7 coronal dimming event for the spectral lines listed in Table 1 TODO: INSERT 1, as well as the GOES 18 Å channel light curve. The leftmost vertical dashed line indicates the GOES event start time, while the other vertical dashed line indicates the GOES event peak time. Peak formation temperature of the EVE spectral lines increases from top to bottom plot. Fe IX to Fe XIII show clear dimming, Fe XIV is borderline, and Fe XV to Fe XX show smooth brightening with no dimming. The Fe XX 131 Å profile is very similar to GOES 18 Å, indicating that this line in EVE is a good proxy for gradual phase timing. Also note the vertical axes: dimming is on the order of a few percent for the cooler Fe emissions while the hotter Fe emissions have bright peaks in the hundreds of percent. All percent changes are calculated from the spectral irradiance at 17:00 UT.

#### 4.1.2 Complex Dimming Case

This event occurred on 2011 August 4 at approximately 3:47 UT. It spawned from NOAA active region 11261 at location N19W36. The eruptive event consisted of an M9.3 flare, a large and fast CME, and nearly all of the types of dimming discussed in Chapter 3: mass-loss and thermal dimming, a global wave that then triggered a sympathetic filament eruption, an obscuration dimming from the filament. This event was chosen specifically for presenting so many types of dimming and related physical processes in a single case.

##### Coronagraph Observations

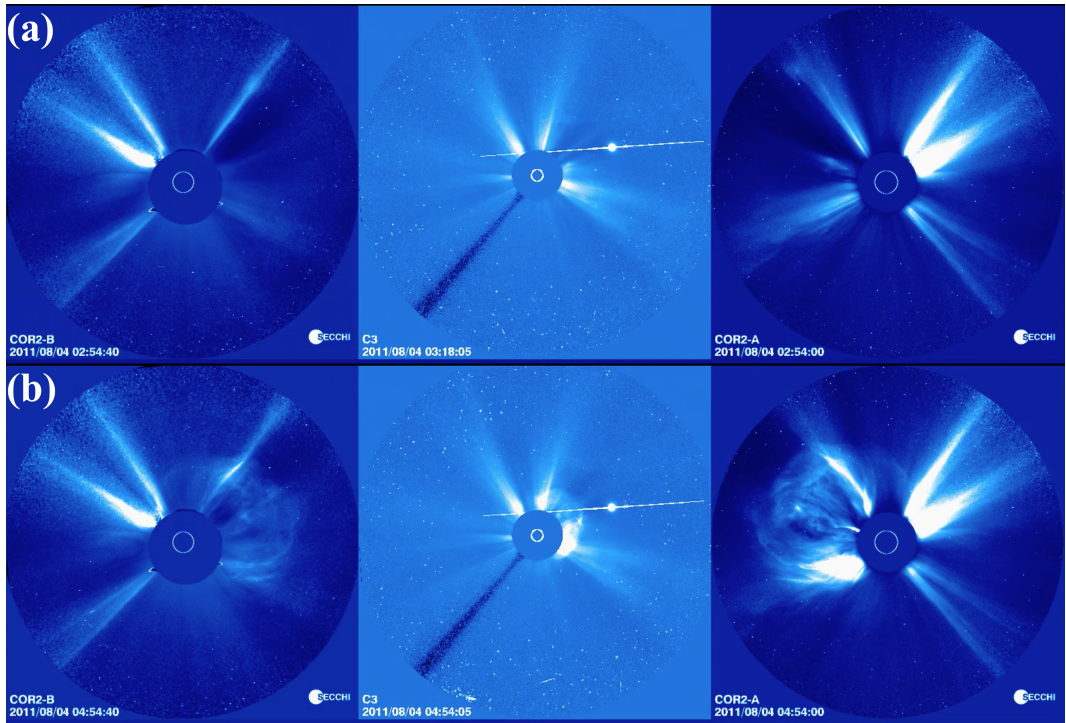


Figure 4.6: CME event associated with 2011 August 4 dimming event. From left to right the coronagraphs are STEREO Behind C2, LASCO C3, and STEREO Ahead C2. Top: Images prior to CME. Bottom: Images during CME.

The CDAW catalog for this event lists it as a halo CME with a velocity of  $1315 \text{ km s}^{-1}$ , relatively fast for a CME, and a mass of  $1.16 \times 10^{16} \text{ g}$ . However, halo CMEs present a strong challenge for obtaining accurate mass, and the catalog flags it as a poor mass estimate. Mass

estimates based on the three coronagraphs are  $8.6 \times 10^{15} g$  for LASCO C3,  $7-8 \times 10^{15} g$  for STEREO-A COR2, and  $4.3 \times 10^{15} g$  for STEREO-B COR2 (A. Vourlidas 2013, private communication). A deprojected, 3-D analysis has not been performed for this CME. Images from the three coronagraphs are shown in Figure 4.6.

The CME in Figure 4.6 (b) can be seen in STEREO-B (behind) on the right of the solar disk, in LASCO as the start of a halo CME offset to the upper-right of the disk, and in STEREO-A (ahead) on the left of the disk. Additionally, bright streamers can be seen inside the CME and on the opposite side of the Sun, signifying that the outer corona of the Sun was also in a more complex configuration than the 2010 August 7 case discussed in Section 4.1.1.

### SDO/AIA EUV Image Observations

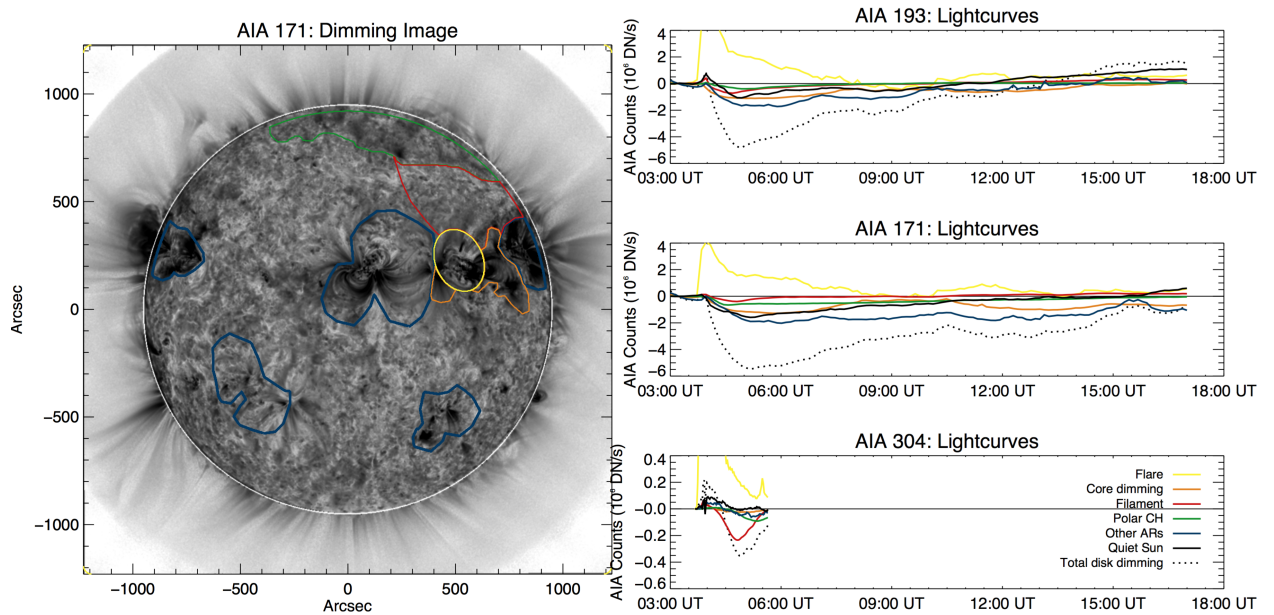


Figure 4.7: Same as Figure 4.3 but for 2010 August 7 event. Colored contours and lines in plots correspond according to legend, but are different from Figure 4.3. An additional difference is that the He II 304 Å line now shows dimming. Not all 304 Å data were available at the time of processing, which is why the time series ends at 6:00 UT. Figure courtesy of Rachel Hock.

The complexity this eruptive event are quite apparent in AIA observations. Figure 4.7 is in the same format as Figure 4.3 but is for the 2011 August 4 event. Dimming is seen in numerous

locations for this event, indicating the far-reaching influence of this eruption. In particular, even though 304 Å data were not processed to the end of the dimming window, the main phase of obscuration dimming is clearly visible. A later figure will show these data in full. Additionally, 193 Å and 171 Å show dimming in every region outside of the flare-isolating contour (yellow). The primary region thought to be associated with mass-loss dimming is labeled "core dimming" (orange) here. It corresponds to an area immediately surrounding the active region where the flare took place and is bounded by loops quiet-Sun on top and bottom and other active region's loops to the left and right. All other active regions visible on disk are contained in blue contours and eventually show even greater dimming than the core region (orange). Note that for the first several minutes, the core dimming dominates the other active regions. Note that the dotted black dash line is the disk signal excluding the flare region (yellow), or effectively the sum of all plotted lines except yellow. It can be seen that the relative contribution of each region to the total dimming is nonzero. Table 4.1 details these contributions.

The overall structure of Table 4.1 is wavelength and feature (vertical) and contribution at maximum dimming (i.e. minimum count), maximum dimming contribution, and the range of contributions. It can be seen that in 193 Å and 171 Å, peak dimming is dominated by the non-flaring active regions. As will be shown later, this is mainly a reflection of the most nearby active region's dimming. It is also worth noting that core dimming reaches its maximum dimming 36 minutes earlier than non-flaring active regions. This suggests that the latter is a sympathetic response to the primary dimming, likely catalyzed by the global wave. As expected, in 304 Å, the minimum count is dominated by the filament. This is consistent with the physical theory for obscuration dimming detailed in Section 3.5. The dominant region changes when looking at the maximum contribution. Here, core dimming dominates for 193 Å but remains the non-flaring active regions still dominate in 171 Å. Again, we will soon show that the most nearby active region contributes greatly to the dimming and may have contributed to the outgoing mass of the CME. 304 Å remains consistent for contribution maximum, with its greatest value coming from the filament eruption. Finally, the range of contributions shows that in 193 Å, core dimming and non-flaring

Table 4.1: Statistics for dimming features in Figure 4.7 for 2011 August 4 event. Table courtesy of Rachel Hock.

Dimming Feature	Time (UT)	Count Counts ( $10^6 DN s^{-1}$ )		Contribution (%)	Time (UT)	Contribution Counts ( $10^6 DN s^{-1}$ )		Contribution (%)	Range of Contribution (%)
		Minimum	Maximum			( $10^6 DN s^{-1}$ )	( $10^6 DN s^{-1}$ )		
<b>AIA 193:</b>									
Total disk dimming	4:55	-4.81	-						
Core dimming	5:17	-1.11	25.3	04:05	-0.63	73.1	18.9-	73.1	
Filament eruption	4:41	-0.72	16.2	04:05	-0.23	27.2	1.0-	27.2	
Polar coronal hole	5:03	-0.39	8.5	05:17	-0.38	8.7	0.6-	8.7	
Non-flaring active regions	5:53	-1.72	43.1	08:04	-1.05	54.6	29.6-	54.6	
Quiet Sun	4:55	-1.07	22.3	08:40	-0.57	26.0	8.0-	26.0	
<b>AIA 171:</b>									
Total disk dimming	5:10	-5.46	-						
Core dimming	5:53	-1.28	24.5	04:05	-0.40	27.3	9.4-	27.3	
Filament eruption	4:48	-0.40	8.0	04:41	-0.38	8.1	0.0-	8.1	
Polar coronal hole	4:34	-0.66	15.7	04:26	-0.63	16.6	7.5-	16.6	
Non-flaring active regions	6:00	-2.02	38.9	08:54	-1.72	53.9	16.6-	53.9	
Quiet Sun	5:10	-1.59	29.0	04:05	-0.68	46.7	20.8-	46.7	
<b>AIA 304:</b>									
Total disk dimming	4:53	-0.36	-						
Core dimming	5:08	-0.03	9.5	04:23	-0.02	62.2	7.4-	62.2	
Filament eruption	4:49	-0.24	69.4	04:25	-0.08	304.3	9.4-	304.3	
Polar coronal hole	5:22	-0.09	40.0	05:38	-0.06	49.3	1.1-	49.3	
Non-flaring active regions	5:11	-0.06	20.6	05:31	-0.05	25.1	2.4-	25.1	
Quiet Sun	5:34	-0.02	14.0	05:37	-0.02	14.4	0.1-	14.4	

active regions are comparable in their dominance; 171 Å's has greater contribution from non-flaring active regions and the quiet-Sun; and 304 Å is very clearly dominated by the filament.

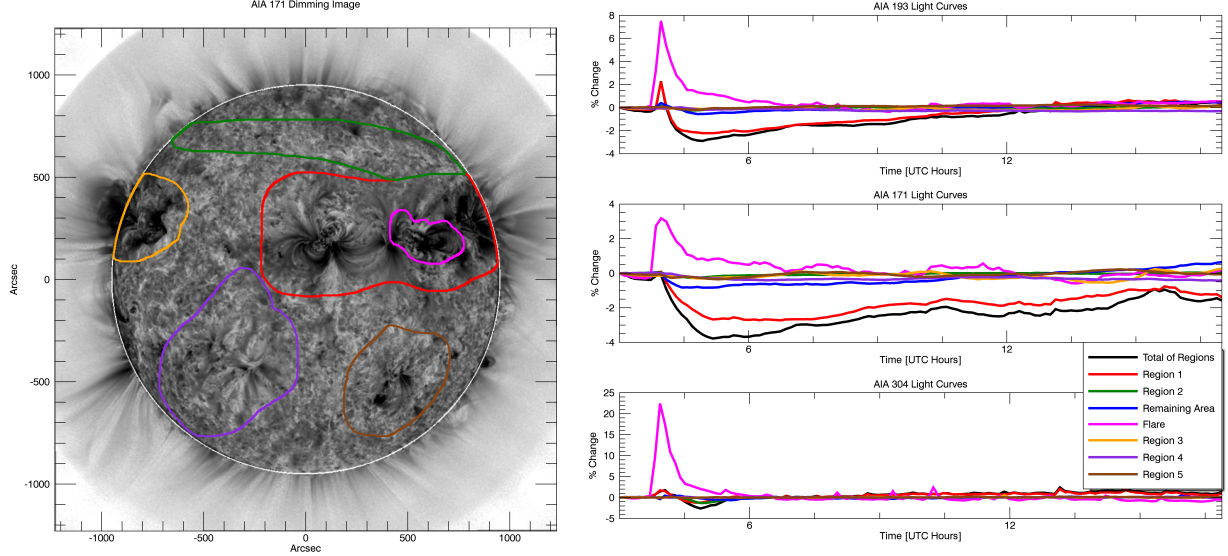


Figure 4.8: Same as Figure 4.7 but with new contours selected and no point spread function correction applied. Also 304 Å data are now complete.

Figure 4.8 is the same format as Figure 4.7 but with different regions selected, and does not use images corrected with the point spread function. The latter explains why the total disk dimming is about 2% less than in Figure 4.7. Of importance here is that the red contour, which encompasses the core dimming region from Figure 4.7 and the most nearby non-flaring active region, accounts for the majority of total dimming in 193 Å and 171 Å. These two active regions are so close together that it is possible that the CME pulled mass away from a coronal volume encompassing both active regions. It can also be seen that 171 Å has a more prominent dimming in the remaining area (blue), i.e. quiet-Sun, than in 193 Å. This is evidence of the type of heat-wave dimming described in Robbrecht and Wang (2010).

We also note that while the AIA 193 Å band contains the Fe XXIV 192 Å emission line, this high ionization state is only expected in hot plasma such as in flaring loops, which are spatially

isolated in the contours of Figures 4.3, 4.7, and 4.8. Thus, for this particular case of spectral blending, the impact on analysis and interpretation is minimized.

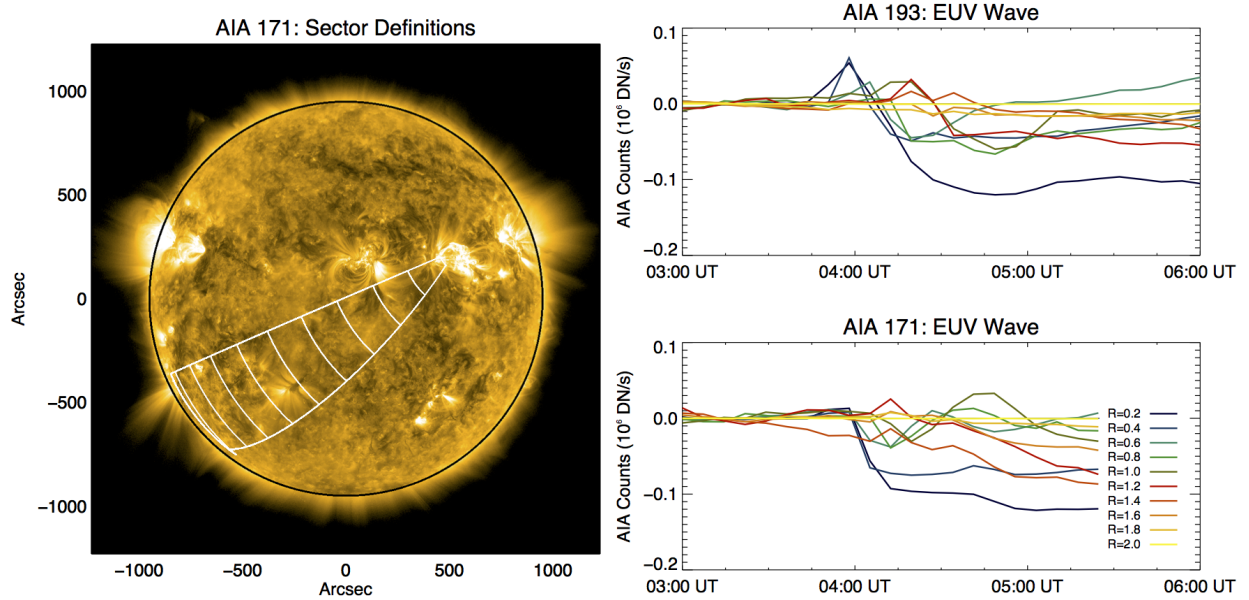


Figure 4.9: Similar format to Figure 4.8, but with geometric contours selected specifically for analysis of propagating wave. In the line plots on the right, distance from the source active region increases with lightness of color. Figure courtesy of Rachel Hock.

Running difference movies make viewing EUV waves easier but it is difficult get the same effect with static images. Instead, Figure 4.9 follows a similar format to earlier AIA figures but draws geometric contours propagating from the source active region specifically for analysis of the EUV wave. The light curves in Figure 4.9 are color coded from dark to light corresponding to increasing distance from the source region. The propagation of the wave can be seen as the dark curves reach their minimum earlier with larger magnitude and the lightest curves show only a minor impact from the wave. This is expected behavior for any impulsive wave phenomenon as energy is dissipated in the surrounding medium.

### SDO/EVE EUV Irradiance Observations

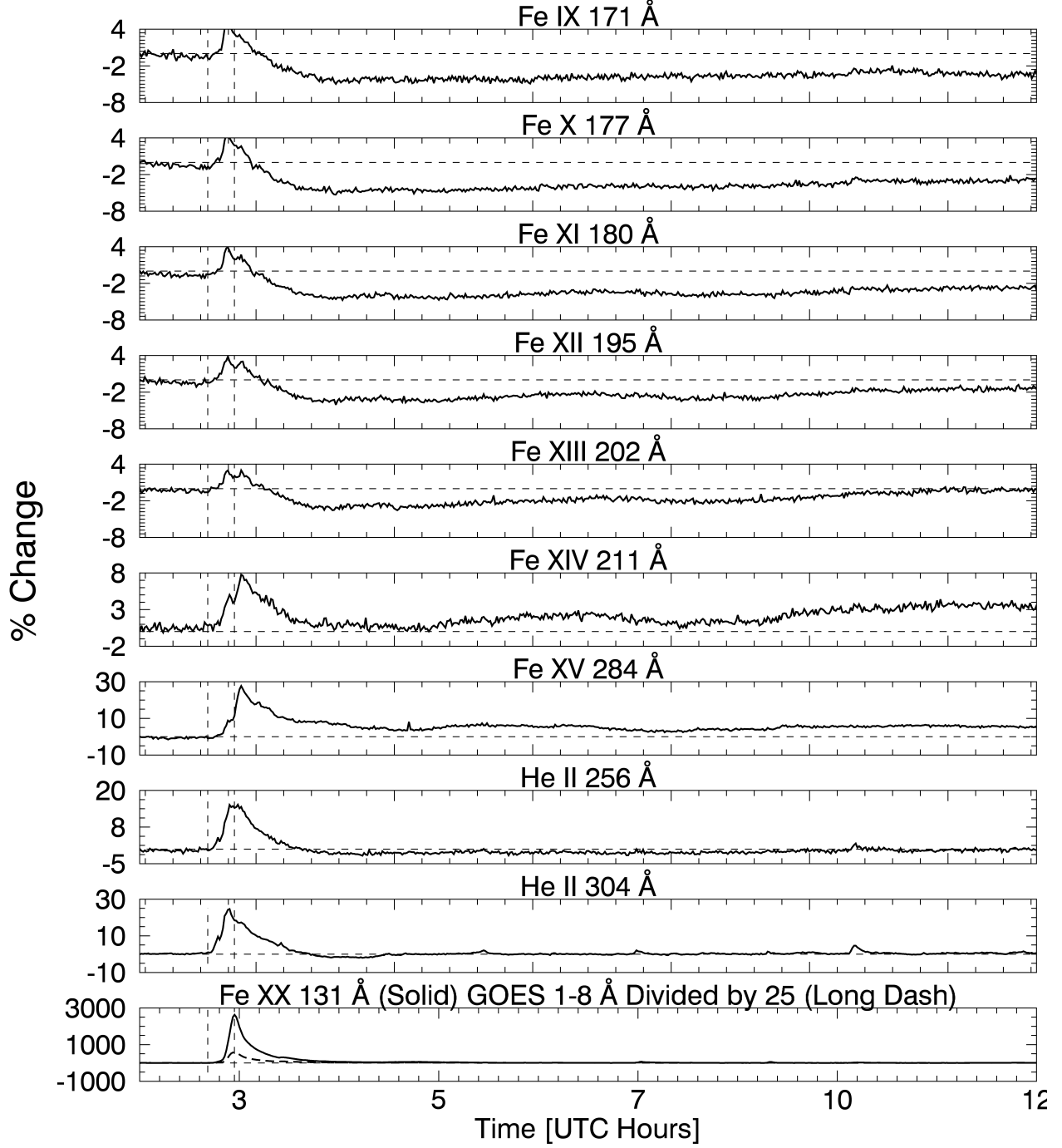


Figure 4.10: Same as Figure 4.5 but for the 2011 August 4 event, and showing He II 256 Å and 304 Å instead of Fe XVI 335 Å and Fe XVIII 94 Å. Just as before, Fe IX to Fe XIII show clear dimming, Fe XIV is borderline, and Fe XV to Fe XX show smooth brightening with no dimming. The Fe XX 131 Å profile is 3x larger than GOES 1-8 Å but still has a similar shape and timing. Also note the vertical axes: dimming is 2x larger than it was for the 2010 August 7 event. The two He II lines show dimming as well, suggestive of obscuration dimming.

Figure 4.10 shows selected extracted emission lines from EVE for the 2011 August 7 complex eruptive event. Because obscuration dimming is important for this case, the plot includes two He II lines: 256 Å and 304 Å, both of which show dimming at approximately the same time as what was seen in AIA (Figure 4.7). The irradiance increase from roughly 5:00 to 7:00 UT in Fe XIV 211 Å may relate to the EUV late phase discussed in Woods et al. (2011). Dimming in Fe IX to Fe XIII was significant in this case, roughly twice as large as in the simpler 2010 August 7 event. Furthermore, the peak time versus ionization state trend is reversed compared to the simpler event e.g., Fe IX 171 Å actually peaks just prior to the GOES event peak time (second vertical dash), and higher ionization states peak later and later. This is indicative that heating processes are dominating the overall irradiance. In either heating or cooling cases, the flare-dimming deconvolution method discussed in Section 4.2 works equally well.

## 4.2 Flare-Dimming Deconvolution Method

Figures 4.5 and 4.10 showed how cooling and heating impact the time of an irradiance peak in each ionization state of Fe: cooling causes the low ionization states to peak later and heating causes the reverse. In either case, it is clear that dimming magnitude decreases with higher ionization states of Fe. Eventually, around Fe XIV at 211 Å, dimming is no longer clear. The next ionization state, Fe XV at 284 Å, shows strong brightening in response to the flare but no dimming. The shape of the flare peak is similar in all wavelengths, though it appears to become more smooth at higher ionization states because of the significantly larger increase making the small oscillations imperceptible in the plots. Using this observation, we developed a simple algorithm to remove the flare peak in the dimming lines. We make the assumption that the peak in the high ionization states is a good proxy for what *would have* been observed in the low ionization states if there were no dimming. However, the magnitudes and timing are quite different. To account for this, we scale the larger peak down and shift it in time so that they are matched. An example of the the impact on the irradiance is shown in Figure 4.11 and a flow-chart of the algorithm is shown in Figure 4.12. The ten-second EVE data are averaged to two-minutes to reduce noise (see black line in Figure

4.11) and the simple IDL *max* function applied to find the peak in the light curve for every emission line listed in Table 4.1. Then, the scaled non-dimming emission line is shifted in time such that its peak matches the one in the dimming line (see green line in Figure 4.11). Finally, the scaled and time-shifted non-dimming light curve is subtracted from the dimming emission line (see blue line in Figure 4.11).

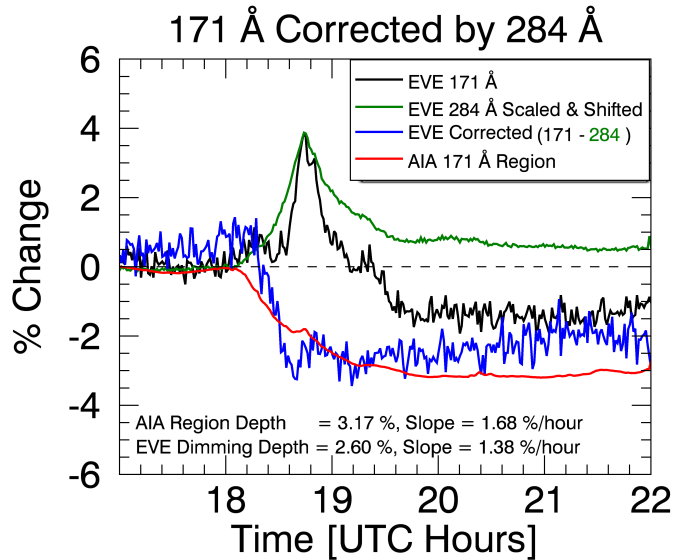


Figure 4.11: Example of the flare-dimming deconvolution method. This particular event is the simple case described in Section 4.1.1. A non-dimming line (e.g., 284 Å) is scaled down and shifted in time such that its flare peak matches the one in a dimming line (green and black, respectively). The scaled and time-shifted non-dimming light curve is then subtracted from the dimming light curve, resulting in a "corrected" or "deconvolved" light curve representative of mass-loss dimming (blue). The red line is the same as the red line in Figure 4.3, indicating the spatially isolated dimming in AIA 171. Dimming depth and slope are shown at the bottom of the plot and were computed at a particular time and time range, respectively.

The red line in Figure 4.11 is the same red line that was in Figure 4.3, which corresponded to the dimming area in AIA thought to be most associated with mass-loss from the corresponding observed CME. It is clear that the deconvolution method applied brings the EVE light curve much closer (from black line to blue line) to the AIA one (red line). The agreement is not perfect, particularly at later times, and the noise in EVE is greater even with the two-minute average than

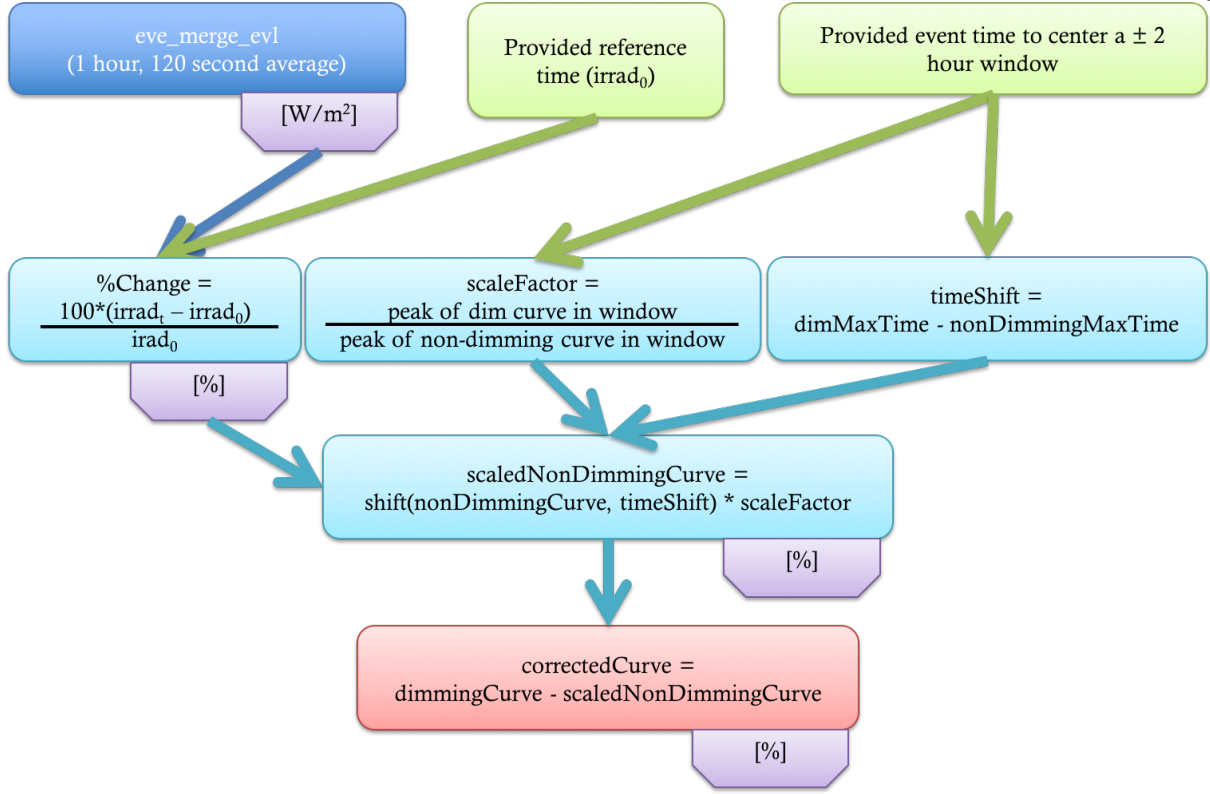


Figure 4.12: Flow-chart for the flare-dimming deconvolution algorithm. Rounded-rectangular boxes describe the steps and the purple boxes indicate the units of the irradiance at that step.

AIA. However, the agreement during the initial decline is much better and is where the slope of dimming is computed, which will be shown to be a critical proxy to CME velocity. The later rise in the corrected EVE line (blue) is due to a slow decrease in the scaled & time-shifted correction line (green). The unaltered dimming line (black) is relatively flat in the later hours of the dimming, consistent with the AIA light curve (red). This behavior varies by event but a "bottomed-out" dimming is common. Typically, the maximum depth is reached quickly and maintained for several hours. It will later be shown that depth is another critical proxy for CMEs; this one for CME mass. In practice, the depth is measured at a point soon after the maximum dimming is reached, so behavior of the corrected EVE line (blue) is of less importance than the removal of the flare peak. Furthermore, the further in time one goes, the more likely it is for other events or physical processes to occur that would complicate the spatially-integrated EVE analysis. Duration of dimming may be

an interesting parameter to study, but due to the continuing evolution and dynamics of the sun it is of secondary priority. Additionally, the duration is likely to be most closely linked to the physical processes responsible for filling plasma back into the void, relaxation of the disturbed system, and temperature evolution changing ionization fractions. All of these have a tenuous connection to CME kinetics and thus provide less promise of providing a physical justification for dimming proxies for CMEs.

Which combinations of dimming and non-dimming line make for the best dimming-isolated light curve? In the simple 2010 August 7 event, it was Fe IX 171 Å (dimming) and Fe XV 284 Å, respectively. In the 28 other cases studied (see Chapter 5), this same combination proved best.

### 4.3 Error Propagation

Coronal dimming is a transient event lasting several hours that is studied in terms of relative change from the initiation time. As such, no long-term degradation of EVE needs to be factored into uncertainties i.e. the absolute accuracy is not important but the measurement precision is most important for the dimming uncertainty. To estimate precision, a period of solar inactivity was analyzed: 2013 January 28 from 00:00–01:00 UT. The estimated precision of these 120-second averaged EVE line data was calculated as the variance of the mean, i.e., the standard deviation divided by the square root of the number of samples, which was 12 in this analysis (?) (pg 73). Table 4.2 provides the estimated precision for each emission line used in this study, and provides a sense of how well we can detect SDO/EVE dimmings that have depths less than 5% of the pre-flight irradiance level.

These base uncertainties were propagated through each step of the EVE dimming correction method described in Section 4.2, which were finally fed as measurement errors into IDLs *poly\_fit* function for fitting the dimming trend. First, the line precisions are combined with the provided

Table 4.2: Estimated precision for selected emission lines in EVE spectra. The Fe IX 171 Å and Fe XV 284 Å emission lines are the choice lines for dimming analysis.

Ion	Wavelength (Å)	Estimated Precision (%)
Fe IX	171	0.06
Fe X	177	0.05
Fe XI	180	0.04
Fe XII	195	0.04
Fe XIII	202	0.04
Fe XIV	211	0.07
Fe XV	284	0.08
Fe XVI	335	0.17
Fe XVIII	94	0.08
Fe XX	132	0.20

reference time to compute percent change (see Figure 4.12, Equation 4.1).

$$\%change = 100 \times \frac{(irrad_t - irrad_0)}{irrad_0} \quad (4.1)$$

where  $irrad_t$  is the irradiance at each time and  $irrad_0$  is the irradiance at the provided reference time. In practice, the latter is a manually selected pre-flare point that appears to correspond well to a quiet or well-behaved period. All of the uncertainty derivations to follow are based on the fundamental uncertainty,

$$F = f(X, Y) \quad (4.2)$$

$$\sigma_F^2 = \sigma_x^2 \left( \frac{\partial F}{\partial X} \right)^2 + \sigma_Y^2 \left( \frac{\partial F}{\partial Y} \right)^2 \quad (4.3)$$

where  $F$  is a generic function that will be specified for each of the steps of the deconvolution method. The first step of computing percent change ( $F$  = Equation 4.1) has the corresponding uncertainty derivation:

$$\begin{aligned}
\frac{\partial F}{\partial X} &= \frac{100}{irrad_0} \implies \left(\frac{\partial F}{\partial X}\right)^2 = \left(\frac{100}{irrad_0}\right)^2 \\
\frac{\partial F}{\partial Y} &= -\frac{100 \times irrad_t}{irrad_0^2} \implies \left(\frac{\partial F}{\partial Y}\right)^2 = \left(-\frac{100 \times irrad_t}{irrad_0^2}\right)^2 \\
\therefore \sigma_F^2 &= \sigma_x^2 \left(\frac{100}{irrad_0}\right)^2 + \sigma_y^2 \left(-\frac{100 \times irrad_t}{irrad_0^2}\right)^2 \\
&\implies \sigma_F = \sqrt{\sigma_x^2 \left(\frac{100}{irrad_0}\right)^2 + \sigma_y^2 \left(-\frac{100 \times irrad_t}{irrad_0^2}\right)^2} \tag{4.4}
\end{aligned}$$

where  $\sigma_x$  is the precision of  $irrad_t$  and  $\sigma_y$  is the precision of  $irrad_0$ , which will be identical in this case as Equation 4.1 refers to a single emission line. This is the uncertainty corresponding to *dimmingCurve* and *NonDimmingCurve*. The next step in the algorithm (Figure 4.12) is to scale the *NonDimmingCurve* irradiance so that the peaks of the dimming and non-dimming line have the same magnitude (both of which are now in % units). The derivation for the corresponding uncertainty is,

$$\begin{aligned}
F &= x \times y \\
\frac{\partial F}{\partial x} &= y, \frac{\partial F}{\partial y} = x \\
\therefore \sigma_F^2 &= \sigma_x^2 y^2 + \sigma_y^2 x^2 = \sigma_{scaledNonDimmingCurve}^2 \tag{4.5}
\end{aligned}$$

where  $x$  is the non-dimming light curve,  $\sigma_x$  is the result of Equation 4.4 (i.e. the  $\sigma_F$  in Equation 4.4),  $y$  is the scale factor (which is a single value), and  $\sigma_y$  is derived as follows:

$$\begin{aligned}
\text{Let } \frac{d}{b} &= \frac{dimCurve_{peak}}{nondimCurve_{peak}} = y \\
\sigma_y^2 &= \sigma_d^2 \left(\frac{1}{b}\right)^2 + \sigma_b^2 \left(-\frac{d}{b^2}\right)^2 \\
\therefore \sigma_y^2 &= \left(\frac{\sigma_d}{b}\right)^2 + \left(\frac{\sigma_b d}{b^2}\right)^2
\end{aligned}$$

Thus we have the *scaledNonDimmingCurve* and its associated propagated uncertainty. The final step is to apply the correction to the *dimmingCurve*, which is just a simple subtraction with the associated uncertainty:

$$\sigma_{correctedCurve} = \sqrt{\sigma_{dimmingCurve}^2 + \sigma_{scaledNonDimmingCurve}^2} \quad (4.6)$$

Figure 3 shows the comparison of the measurement errors and the resultant  $1\sigma$  uncertainties computed by *poly\_fit*. The fits achieve the desired effect of reducing uncertainty even further and providing a smooth function to parameterize.

## 4.4 Dimming and CME Parameterization Results

### 4.4.1 Simple Dimming Case

### 4.4.2 Complex Dimming Case

## 4.5 Summary

## **Chapter 5**

### **Semi-Statistical Study of Coronal Dimming**

## **Chapter 6**

### **Overview of MinXSS Solar CubeSat**

## **Chapter 7**

### **Thermal Balance Analysis for a CubeSat**

## **Chapter 8**

### **Summary and Future Work**

## Bibliography

- Andretta, V., Del Zanna, G., and Jordan, S. D. (2003). The EUV helium spectrum in the quiet Sun: A by-product of coronal emission? *Astronomy and Astrophysics*, 400(2):737–752.
- Aschwanden, M. J., Nitta, N. V., Wuelser, J.-P., Lemen, J. R., Sandman, A., Vourlidas, A., and Colaninno, R. C. (2009). First Measurements of the Mass of Coronal Mass Ejections From the EUV Dimming Observed With Stereo EUVI A + B Spacecraft. *The Astrophysical Journal*, 706(1):376–392.
- Attrill, G. D. R., Harra, L. K., van Driel-Gesztelyi, L., and Wills-Davey, M. J. (2010). Revealing the Fine Structure of Coronal Dimmings and Associated Flows with Hinode/EIS. *Solar Physics*, 264(1):119–147.
- Caspi, A., McTiernan, J. M., and Warren, H. P. (2014). CONSTRAINING SOLAR FLARE DIFFERENTIAL EMISSION MEASURES WITH EVE AND RHESSI. *The Astrophysical Journal*, 788(2):L31.
- Chen, P. F., Fang, C., and Shibata, K. (2005). A Full View of EIT Waves. *The Astrophysical Journal*, 622(2):1202–1210.
- Chen, P. F., Wu, S. T., Shibata, K., and Fang, C. (2002). Evidence of EIT and Moreton Waves in Numerical Simulations. *The Astrophysical Journal*, 572(1):L99–L102.
- Colaninno, R. C. and Vourlidas, A. (2009). First Determination of the True Mass of Coronal Mass Ejections: A Novel Approach To Using the Two Stereo Viewpoints. *The Astrophysical Journal*, 698:852–858.
- Fletcher, L., Dennis, B. R., Hudson, H. S., Krucker, S., Phillips, K., Veronig, A. M., Battaglia, M., Bone, L., Caspi, A., Chen, Q., Gallagher, P. T., Grigis, P. T., Ji, H., Liu, W., Milligan, R. O., and Temmer, M. (2011). An Observational Overview of Solar Flares. *Space Science Reviews*, 159(1-4):19–106.
- Gilbert, H. R., Inglis, a. R., Mays, M. L., Ofman, L., Thompson, B. J., and Young, C. a. (2013). Energy Release From Impacting Prominence Material Following the 2011 June 7 Eruption. *The Astrophysical Journal*, 776(1):L12.
- Giordano, S., Antonucci, E., and Dodero, M. (2000). OXYGEN VELOCITIES IN A POLAR CORONAL. *Advances in Space Research*, 25(9):1927–1930.

- Gopalswamy, N., Yashiro, S., Michalek, G., Stenborg, G., Vourlidas, A., L, F. S., and Howard, R. A. (2009). The SOHO / LASCO CME Catalog. *Earth Moon Planet*, 104:295–313.
- Greenstein, J. L. (1958). High-Resolution Spectra of Comet MRKOS. *The Astrophysical Journal*, 128:106.
- Harra, L. K., Mandrini, C. H., Dasso, S., Gulisano, A. M., Steed, K., and Imada, S. (2010). Determining the Solar Source of a Magnetic Cloud Using a Velocity Difference Technique. *Solar Physics*, 268(1):213–230.
- Harra, L. K. and Sterling, A. C. (2001). Material Outflows from Coronal Intensity "Dimming Regions" During Coronal Mass Ejection Onset. *The Astrophysical Journal Letters*, 561:215–218.
- Harrison, R. A., Bryans, P., Simnett, G. M., and Lyons, M. (2003). Coronal dimming and the coronal mass ejection onset. *Astronomy & Astrophysics*, 400:1071–1083.
- Harrison, R. A. and Lyons, M. (2000). A spectroscopic study of coronal dimming associated with a coronal mass ejection. *Astronomy & Astrophysics*, 1108:1097–1108.
- Hudson, H. S., Woods, T. N., Chamberlin, P. C., Fletcher, L., Zanna, G. D., Didkovsky, L., Labrosse, N., and Graham, D. (2011). The EVE Doppler Sensitivity and Flare Observations. *Solar Physics*, 273:69–80.
- Hyder, C. L. and Lites, B. W. (1970). H-alpha Doppler Brightening and Lyman-alpha Doppler Dimming in Moving H-alpha Prominences. *Solar Physics*, 14(1):147–156.
- Imada, S., Hara, H., Watanabe, T., Kamio, S., Asai, A., Matsuzaki, K., Harra, L. K., and Mariska, J. T. (2007). Discovery of a Temperature-Dependent Upflow in the Plage Region during a Gradual Phase of the X-Class Flare. *Publications of the Astronomical Society of Japan*, 59(sp3):S793–S799.
- Jin, M., Ding, M. D., Chen, P. F., Fang, C., and Imada, S. (2009). CORONAL MASS EJECTION INDUCED OUTFLOWS OBSERVED WITH HINODE /EIS. *The Astrophysical Journal*, 702(1):27–38.
- Labrosse, N. and Mcglinchey, K. (2012). Plasma diagnostic in eruptive prominences from SDO / AIA observations at 304 Å. *Astronomy & Astrophysics*, 537:A100.
- Liu, W. and Ofman, L. (2014). Advances in Observing Various Coronal EUV Waves in the SDO Era and Their Seismological Applications (Invited Review). *Solar Physics*, 289(9):3233–3277.
- Mason, J. P., Woods, T. N., Caspi, A., Thompson, B. J., and Hock, R. A. (2014). MECHANISMS AND OBSERVATIONS OF CORONAL DIMMING FOR THE 2010 AUGUST 7 EVENT. *The Astrophysical Journal*, 789(1):61.
- Muhr, N., Veronig, A. M., Kienreich, I. W., and Temmer, M. (2011). Analysis of Characteristic Parameters of Large-Scale Coronal Waves Observed by the Solar-Terrestrial Relations Observatory/Extreme Ultraviolet Imager. *The Astrophysical Journal*, 89:89.
- Pohjolainen, S., Vilmer, N., Khan, J. I., and Hillaris, A. E. (2005). Early signatures of large-scale field line opening Multi-wavelength analysis of features connected with a halo CME event. *Astronomy & Astrophysics*, 434:329–341.

- Reinard, A. A. and Biesecker, D. A. (2008). Coronal Mass Ejection-Associated Coronal Dimmings. *The Astrophysical Journal*, 674:576–585.
- Reinard, A. A. and Biesecker, D. A. (2009). The Relationship Between Coronal Dimming and Coronal Mass Ejection Properties. *The Astrophysical Journal*, 705(1):914–919.
- Robbrecht, E. and Wang, Y.-M. (2010). The Temperature-Dependent Nature of Coronal Dimmings. *The Astrophysical Journal Letters*, 720:88–92.
- Rompolt, . (1967). The H $\alpha$  Radiation Field in the Solar Corona for Moving Prominences. *Acta Astronomica*, 17.
- Schrijver, C. J. and Higgins, P. A. (2015). A Statistical Study of Distant Consequences of Large Solar Energetic Events. *Solar Physics*, 290(10):2943–2950.
- Sterling, A. C. and Hudson, H. S. (1997). YOHKOH SXT OBSERVATIONS OF X-RAY DIMMING ASSOCIATED WITH A HALO CORONAL MASS EJECTION. *The Astrophysical Journal*, 491:L55–L58.
- Swings, P. (1941). Complex Structure of Cometary bands Tentatively Ascribed to the Contour of the Solar Spectrum. *Lick Observatory Bulletin*, 508.
- Tian, H., McIntosh, S. W., Xia, L., He, J., and Wang, X. (2012). What Can We Learn About Solar Coronal Mass Ejections, Coronal Dimmings, and Extreme-Ultraviolet Jets Through Spectroscopic Observations? *The Astrophysical Journal*, 748(2):106.
- Woods, T. N., Hock, R. A., Eparvier, F. G., Jones, A. R., Chamberlin, P. C., Klimchuk, J. A., Didkovsky, L., Judge, D., Mariska, J. T., Warren, H. P., Schrijver, C. J., Webb, D. F., Bailey, S. M., and Tobiska, W. K. (2011). New Solar Extreme-Ultraviolet irradiance Observations During Flares. *The Astrophysical Journal*, 739:59.
- Zhukov, A. N. and Auchère, F. (2004). On the nature of EIT waves, EUV dimmings and their link to CMEs. *Astronomy & Astrophysics*, 427:705–716.

## Appendix A

### Coronal Dimming Event List and Ancillary Data

**About appendices:** Each appendix follow the same page-numbering rules as a regular chapter; the first page of a (multi-page) appendix is not numbered. By the way, the following are supposedly authentic answers to English GCSE exams!

- (1) The Greeks were a highly sculptured people, and without them we wouldn't have history.  
The Greeks also had myths. A myth is a female moth.
- (2) Actually, Homer was not written by Homer but by another man of that name.
- (3) Socrates was a famous Greek teacher who went around giving people advice. They killed him. Socrates died from an overdose of wedlock. After his death, his career suffered a dramatic decline.
- (4) Julius Caesar extinguished himself on the battlefields of Gaul. The Ides of March murdered him because they thought he was going to be made king. Dying, he gasped out: Tee hee, Brutus.
- (5) Nero was a cruel tyranny who would torture his subjects by playing the fiddle to them.
- (6) In midevil times most people were alliterate. The greatest writer of the futile ages was Chaucer, who wrote many poems and verses and also wrote literature.
- (7) Another story was William Tell, who shot an arrow through an apple while standing on his sons head.

- (8) Writing at the same time as Shakespeare was Miguel Cervantes. He wrote Donkey Hote. The next great author was John Milton. Milton wrote Paradise Lost. Then his wife died and he wrote Paradise Regained.
- (9) During the Renaissance America began. Christopher Columbus was a great navigator who discovered America while cursing about the Atlantic. His ships were called the Nina, the Pinta, and the Santa Fe.
- (10) Gravity was invented by Issac Walton. It is chiefly noticeable in the autumn when the apples are falling off the trees.
- (11) Johann Bach wrote a great many musical compositions and had a large number of children. In between he practiced on an old spinster which he kept up in his attic. Bach died from 1750 to the present. Bach was the most famous composer in the world and so was Handel. Handel was half German half Italian and half English. He was very large.
- (12) Soon the Constitution of the United States was adopted to secure domestic hostility. Under the constitution the people enjoyed the right to keep bare arms.
- (13) The sun never set on the British Empire because the British Empire is In the East and the sun sets in the West.
- (14) Louis Pasteur discovered a cure for rabbis. Charles Darwin was a naturalist who wrote the Organ of the Species. Madman Curie discovered radio. And Karl Marx became one of the Marx brothers.

## Appendix B

### MinXSS CubeSat Mass/Power Tables

**(Data, Stardate 1403827)** (A one-page chapter — page must be numbered!) Throughout the ages, from Keats to Giorchamo, poets have composed “odes” to individuals who have had a profound effect upon their lives. In keeping with that tradition I have written my next poem . . . in honor of my cat. I call it . . . Ode . . . to Spot. (Shot of Geordi and Worf in audience, looking mystified at each other.)

Felus cattus, is your taxonomic nomenclature  
 an endothermic quadruped, carnivorous by nature?  
 Your visual, olfactory, and auditory senses  
 contribute to your hunting skills, and natural defenses.  
 I find myself intrigued by your sub-vocal oscillations,  
 a singular development of cat communications  
 that obviates your basic hedonistic predilection  
 for a rhythmic stroking of your fur to demonstrate affection.  
 A tail is quite essential for your acrobatic talents;  
 you would not be so agile if you lacked its counterbalance.  
 And when not being utilized to aid in locomotion,  
 It often serves to illustrate the state of your emotion.

(Commander Riker begins to applaud, until a glance from Counselor Troi brings him to a halt.) Commander Riker, you have anticipated my denouement. However, the sentiment is appreciated. I will continue.

O Spot, the complex levels of behavior you display  
 connote a fairly well-developed cognitive array.  
 And though you are not sentient, Spot, and do not comprehend  
 I nonetheless consider you a true and valued friend.

## Appendix C

### MinXSS Thermal Model Parameter Tables

**(Data, Stardate 1403827)** (A one-page chapter — page must be numbered!) Throughout the ages, from Keats to Giorchamo, poets have composed “odes” to individuals who have had a profound effect upon their lives. In keeping with that tradition I have written my next poem . . . in honor of my cat. I call it . . . Ode . . . to Spot. (Shot of Geordi and Worf in audience, looking mystified at each other.)

Felus cattus, is your taxonomic nomenclature  
an endothermic quadruped, carnivorous by nature?  
Your visual, olfactory, and auditory senses  
contribute to your hunting skills, and natural defenses.  
I find myself intrigued by your sub-vocal oscillations,  
a singular development of cat communications  
that obviates your basic hedonistic predilection  
for a rhythmic stroking of your fur to demonstrate affection.  
A tail is quite essential for your acrobatic talents;  
you would not be so agile if you lacked its counterbalance.  
And when not being utilized to aid in locomotion,  
It often serves to illustrate the state of your emotion.

(Commander Riker begins to applaud, until a glance from Counselor Troi brings him to a halt.)  
Commander Riker, you have anticipated my denouement. However, the sentiment is appreciated.  
I will continue.

O Spot, the complex levels of behavior you display  
connote a fairly well-developed cognitive array.  
And though you are not sentient, Spot, and do not comprehend  
I nonetheless consider you a true and valued friend.